Analysis of a Small, Vigorous Mesoscale Convective System in a Low-Shear Environment. Part II: Evolution of the Stratiform Precipitation and Mesoscale Flows

KEVIN R. KNUPP AND BART GEERTS*

Earth System Science Laboratory, University of Alabama in Huntsville, Huntsville, Alabama

JOHN D. TUTTLE

National Center for Atmospheric Research, Boulder, Colorado

(Manuscript received 13 December 1996, in final form 23 June 1997)

ABSTRACT

The evolution of the mesoscale flow and precipitation distribution are investigated for a small mesoscale convective system (MCS) that evolved in a nearly barotropic environment exhibiting moderate instability and weak wind shear. Observations primarily from a single Doppler radar detail the growth of the MCS from the merger of several clusters and lines of vigorous convective cells into a mature state consisting of a weaker convective line trailed by an expanding stratiform precipitation region. Analysis of radar reflectivity reveals that this stratiform region formed in situ in the presence of weak mesoscale updraft as decaying convective cores coalesced, rather than through rearward advection of ice particles directly from the convective region. In the absence of sufficient low-level shear, the MCS collapsed rapidly as it assumed the structure of the archetypal convective line and trailing stratiform precipitation region.

Velocity–azimuth displays reveal mesoscale updrafts of about 70 cm s^{-1} during the active convective stage. In the mature stratiform region, the lower-tropospheric mesoscale downdraft ($\sim$40 cm s^{-1}) exceeded the mesoscale updraft ($\sim$10 cm s^{-1}) above it, and the level separating the two was relatively high at 6.5 km, about 2 km above the 0°C level. As the MCS cloud-top anvil area colder than −52°C peaked near 60 000 km^2, the cloud top descended at rates of 20–40 cm s^{-1} despite weak but sustained mesoscale updraft within the upper part of the cloud.

A rear inflow jet was observed before convective activity peaked, remained strong while the deep convection diminished, and became the main flow feature as the MCS decayed. This jet subsided from approximately 7 km at the rear end to near the surface at the leading edge of the convection. A weaker ascending front-to-rear current was found above this rear inflow jet.

No midlevel mesoscale cyclonic vortex was apparent in the echo structure of the maturing MCS. Indirect estimates of mesoscale vorticity, based on Lagrangian conservation of radar reflectivity, indicate that cyclonic rotation was present in the mesoscale downdraft region, and anticyclonic rotation occurred aloft. The magnitude of this vorticity is about half the Coriolis parameter. A positive potential vorticity anomaly is found at midlevels within the MCS, and this anomaly intensifies in depth and in strength as the system matures. This growth is consistent with the diabatic heating profile estimated from a 1D cloud model.

1. Introduction

In Part I of this series (Knupp et al. 1998), we examined the evolution of radar reflectivity factor *Z*, precipitation, cloud-to-ground lightning, and cloud-top behavior of a small mesoscale convective system (MCS) that formed in a weakly sheared, moderately unstable environment near the Alabama–Tennessee border. We present evidence suggesting that the spatial organization of deep convection was largely controlled by the shallow cloud structure in the prestorm environment. Most rainfall resulted from vigorous, transient thunderstorm cells, while the stratiform precipitation was estimated to contribute less than 20% of the total precipitation. Part I also documents the MCS development through the merger of several lines and clusters of convective cells. The radar analysis suggested that the stratiform region evolved locally, not through the rearward advection from the leading convective line. In this paper, we quantify this finding with additional analyses of *Z*, mesoscale flow fields, and diagnostic retrieval calculations.

Detailed observations of the full three-dimensional structure of MCSs have mostly been limited to the ma-

* Current affiliation: Embry-Riddle Aeronautical University, Prescott, Arizona.

Corresponding author address: Dr. Kevin R. Knupp, University of Alabama in Huntsville, Huntsville, AL 35899.
E-mail: kevin@atmos.uah.edu

ture or decaying states, and few studies document their fourth dimension, that is, the evolution from inception to maturity. This is in part because most of the MCSs studied previously were either too large or too long lived to be fully captured by mesoscale networks. The Cooperative Huntsville Meteorological Experiment mesoscale data network, including the CP-4 radar, fortuitously covered most of this MCS during its entire life cycle on 13 July 1986 (Figs. I.4 and I.12).[1] Here we use these rather unique circumstances to examine how the mesoscale flow field evolved during the metamorphosis of scattered convection into an organized, small MCS.

The general objective of this study is to detail the kinematic and Z_e structure of a small MCS that developed in a nearly barotropic environment with little low-level shear, insufficient to offset the growing strength of the surface cold pool (Rotunno et al. 1988). This specific objective has three specific components. Similar to some larger, longer-lived MCSs, such as the 10–11 June 1985 case (e.g., Biggerstaff and Houze 1993), this MCS had in its mature stage a trailing stratiform region that was separated from a leading squall line by a transition zone. In contrast to some larger systems, the stratiform region in this system formed primarily as a result of in situ decay and upper-level expansion of multiple lines of convection, and it collapsed rapidly, suggesting that it was not supported by a substantial upper-level mesoscale updraft. A first specific objective of this study is to detail the kinematic and cloud microphysical characteristics of the stratiform region during its formation, expansion, and collapse.

Diagnostic and modeling studies of squall lines with a trailing stratiform region have documented a current of air entering at midlevels into the rear of the stratiform region and slowly subsiding toward the leading convective line in a storm-relative frame (Smull and Houze 1987a,b; Fovell and Ogura 1988; Zhang and Gao 1989). This current, which is defined as the rear inflow, can be present even in the early stages of MCS development (Klimowski 1994) and appears to accelerate both in time and toward the leading convective line (Chong et al. 1987). Rear inflow currents range from a broad, subsiding layer of weak inflow to a narrow, strong jet. Some MCSs lack a rear inflow (Smull and Houze 1987a). A second specific objective of this study is to examine the characteristics and genesis of a rear inflow current in a small, unsteady MCS.

Some mature MCSs assume an asymmetric appearance, with a well-defined trailing stratiform region to the left of the storm motion vector of the squall line (Houze et al. 1990; Smull and Augustine 1993). At least in some cases such asymmetry is associated with a cyclonic midlevel mesoscale convective vortex (MCV) centered in the stratiform region (Brandes 1990). MCVs have been documented in a range of sizes, from about 20 km (Verlinde and Cotton 1990) to 200 km (Bosart and Sanders 1981). The smaller ones appear to be shear induced and do not leave behind a mesovortex signature once the convection has ceased. They appear as a cyclonic–anticyclonic couplet around a strong rear inflow jet or, in the presence of strong midlevel shear, on both sides of an updraft core. Such small vortices are short lived because they are smaller than the Rossby radius of deformation, which implies that they are not inertially stable (Verlinde and Cotton 1990).

The larger MCVs appear to be due to the same mechanism that initiates a midlevel cyclonic circulation in tropical depressions. The latent cooling in the low-level mesoscale downdraft and latent heating in the mesoscale updraft at middle and upper levels are consistent with a midlevel cyclonic potential vorticity anomaly (Raymond and Jiang 1990; Fritsch et al. 1994). Skamarock et al. (1994) show that the numerically simulated midlevel MCV in the stratiform region of an asymmetric squall-line system results from the tilting of baroclinically generated horizontal vorticity. At first there is a weak vortex couplet at opposite ends of the squall line, but only the cyclonic one on the left is amplified by midlevel mesoscale convergence, on account of the planetary vorticity f.

The MCS in this study did not display appreciable cyclonic rotation in its echo patterns and was relatively small and short lived compared to the systems in which a stable midlevel MCV has been documented. A third specific objective, then, is to describe the evolution of the mesoscale profiles of relative vorticity, potential vorticity, and latent heating in the case of this relatively small MCS.

The development of the stratiform precipitation is documented in sections 2 and 3 by means of a detailed comparison of radar reflectivity sections and a sequence of velocity–azimuth display (VAD) profiles. The inferred cloud structure is described in section 4, and questions regarding cloud-top vertical motion are addressed in section 5. Detailed analyses of the rear inflow jet and the mesoscale vorticity structure are presented in sections 6 and 7, respectively.

2. Development of stratiform precipitation

In Part I the temporal and spatial characteristics of the expanding stratiform region and associated anvil of the 13 July 1986 MCS were described using radar, Geostationary Operational Environmental Satellite (GOES), and lightning data. Horizontal sections of equivalent reflectivity factor Z_e shown in Fig. 1 portray this growth. In this section we quantify the evolution of the stratiform region associated with the core of convective line B (the major component of the MCS during this time), which exhibited an archtypical squall line

[1] In this paper, Fig. I.*n* refers to Fig. *n* in part I (Knupp et al. 1998); similarly for section I.*n*.

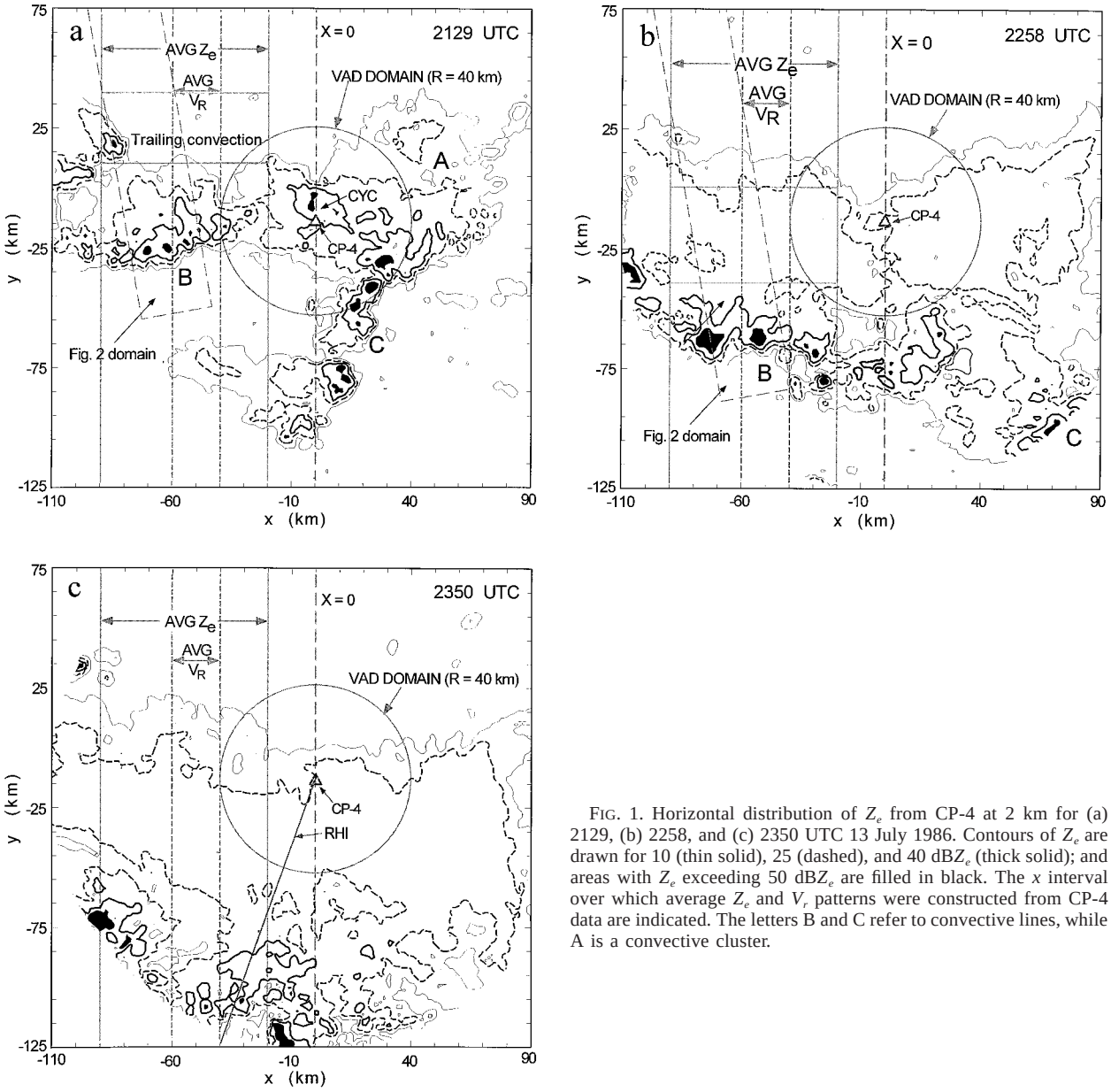

FIG. 1. Horizontal distribution of Z_e from CP-4 at 2 km for (a) 2129, (b) 2258, and (c) 2350 UTC 13 July 1986. Contours of Z_e are drawn for 10 (thin solid), 25 (dashed), and 40 dBZ_e (thick solid); and areas with Z_e exceeding 50 dBZ_e are filled in black. The x interval over which average Z_e and V_r patterns were constructed from CP-4 data are indicated. The letters B and C refer to convective lines, while A is a convective cluster.

structure with a leading convective line and a trailing stratiform region. A sustained horizontal expansion of stratiform precipitation started near 2120 UTC, about 4 h after initial deep convection. This expansion is quantified through analyses of Z_e from 29 low-elevation plan position indicator (PPI) scans from the CP-4 radar over a 30-km-wide swath (defined in Fig. 1) for the 2051–2343 UTC period, presented in time–distance format in Fig. 2. This analysis clearly shows a rapid in situ growth of stratiform precipitation beginning near 2120 UTC, and a subsequent rearward expansion at a rate of 11 m s^{-1} relative to the advancing convective line between 2130 and 2330 UTC.

In the following, we present additional analyses of stratiform precipitation development. The discussion is separated into two time periods, one when the stratiform precipitation was developing (2130–2148 UTC), and the other when the stratiform region was maturing (2258–2335 UTC). The echo structure at the beginning of both time periods is shown in Fig. 1. Time differencing of Z_e between two times is used to calculate rates of Z_e growth.

a. Initial development

The initial development of stratiform precipitation is quantified by performing east–west averages of Z_e over a subset of the domain shown in Fig. 1. In Fig. 3 the

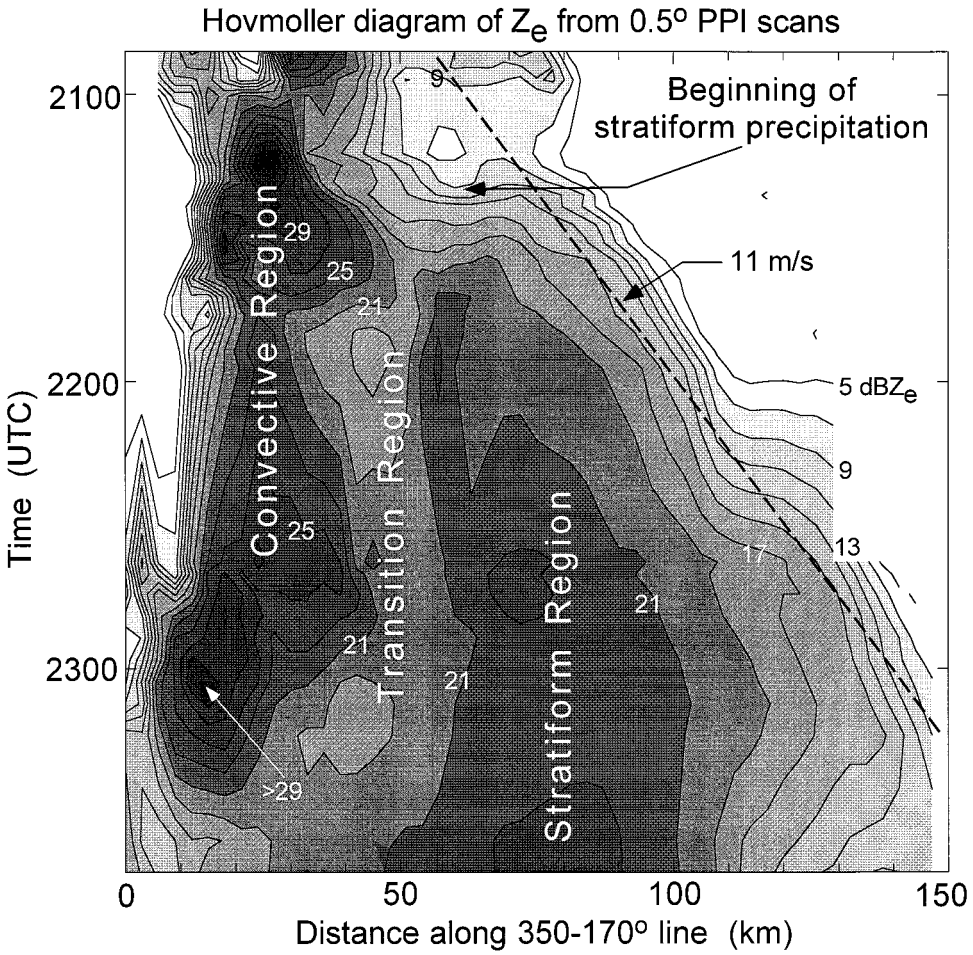

FIG. 2. Hovmöller diagram of reflectivity factor averaged over a 30-km-wide slab obtained from 29 0.5° PPI scans over the 2051–2343 UTC period. Approximate slab locations are indicated in Fig. 1. The slab was moved southward at 5 m s^{-1} to keep convective line B stationary. Stratiform precipitation emerges near 2120 UTC and expands rearward at a rate of 11 m s^{-1} relative to the convective line between 2130 and 2330 UTC.

large contribution of Z_e from the isolated trailing convective cells (Fig. 1a) during the 2130–2148 UTC time period is eliminated. The modified average sections indicate an in situ intensification and expansion of Z_e both toward the front and the rear over this 18-min period. The time difference in Z_e, that is, DIFF (dB) = d-BZ_{av}(2148) − dBZ_{av}(2130), where Z_{av} is the average of linear Z_e over a 70-km width (see section 6d, part I), is presented in Fig. 4a to quantify the magnitude of inferred local intensification. The southward translation of convective line B by about 5 km during the 18-min period has not been removed from the difference field. To accurately calculate the difference, we carefully evaluated signal attenuation [following the technique by Knupp and Chandrasekar (1993)], since the location of CP-4 in the DIFF field along the convective line (Fig. 1a) can introduce errors due to C-band attenuation, which exceeded 10 dB in this case. Of particular importance during this time period is the presence of relatively intense precipitation just to the west of CP-4 (Fig. 1a).

Relatively high DIFF values of 5–10 dB are analyzed in a horizontal layer centered at a height near 4 km, just below the melting level. A second peak located at middle levels near (y, z) = (50, 9) in Fig. 4a results from northward horizontal transport in the anvil outflow. When the translation speed of convective cells (5 m s^{-1}) within the north–south direction is removed from the DIFF field, this second peak increases to about 10 dB. Negative differences at the southern end of Fig. 4a are due to the southward motion of the convective region, which is beyond the left border of Fig. 4a. Considerable structure is apparent in the patterns of negative difference, which are indicative of transient features in the convective region.

The development of the stratiform region is clarified by the profile of the DIFF field within the central portion of the stratiform region (Fig. 5a). Large positive values

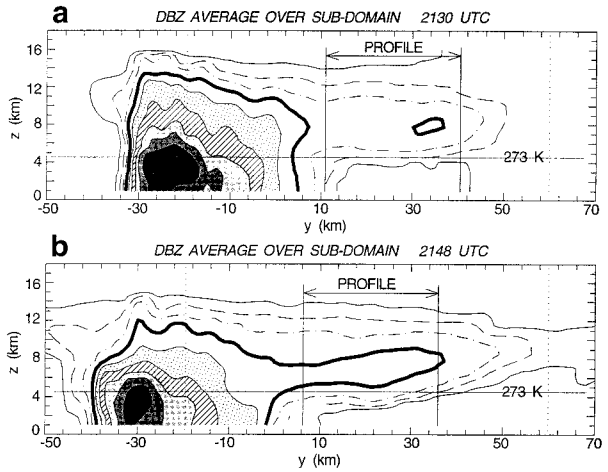

FIG. 3. Average reflectivity patterns through convective line B over the 70-km-wide domain shown in Fig. 1 at (a) 2130 UTC and (b) 2148 UTC, after eliminating the trailing convective cells shown in Fig. 1a. Contours are drawn every 5 dB beginning at 5 dBZ_e (solid line). The vertical dotted lines represent the horizontal domain of the difference calculation of Fig. 4. Vertical profiles averaged over the *y* interval labeled as ''PROFILE'' are shown in Fig. 5.

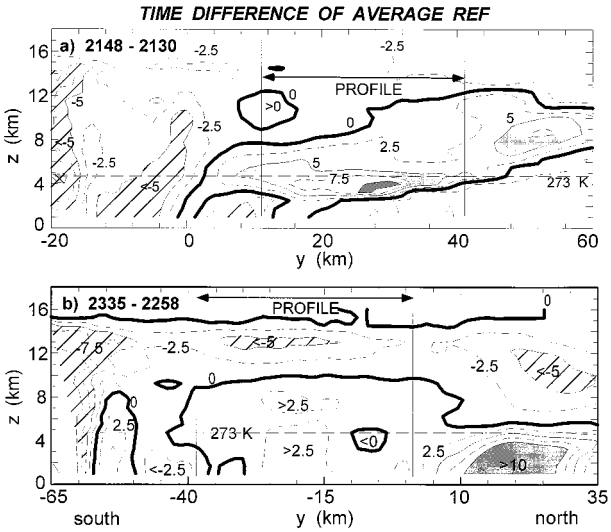

FIG. 4. (a) Difference field (dB) between the average reflectivity factor at 2148 and 2130 UTC (Fig. 1). (b) Same as Fig. 4a but for 2258 and 2335 UTC (Fig. I.18d,e). A vertical profile within the *y* interval labeled as ''PROFILE'' is displayed in Figs. 5a and 5b, respectively. Bold lines represent values of zero difference. Areas of significant increase (>5 dB) are shaded, and areas of significant decrease (>5 dB) are hatched.

in the average DIFF are located within the layer between 3 and 6 km above ground level (AGL). The peak of 7 dB at $z = 4$ km results from downward settling of hydrometeors and the formation of a radar bright band as the snow falling to the freezing level is less rimed at the later time. The increase in DIFF just above the melting level is attributed aggregation of snow within the $-10°$ to 0°C temperature interval (Yeh et al. 1986). The aggregation process, which has yet to be incorporated in cloud microphysical retrieval models (e.g., Rutledge and Houze 1987; Ziegler 1988), affects only the size distribution of hydrometeors, not their mixing ratio. The much smaller increase in Z_e between 6 and 9 km ($-26°C < T < -8°C$) is consistent with growth of ice crystals mainly by vapor deposition. We demonstrate in section 3 that much of the increase in Z_e between 3 and 9 km over this 18-min period occurs *locally* by several microphysical effects, in response to a mesoscale updraft. The negative values in DIFF above 11 km where Z_e is in the range 0–10 dBZ_e can be explained as a net descent of ice crystals.

b. Further growth during the mature phase

For comparison, a similar difference calculation was completed for the 2258–2335 UTC period, which represents a more advanced stage of the stratiform region. The stratiform region was still expanding and intensifying at this time (Figs. 1b,c and 2). The average Z_e sections used in this difference are shown in Fig. I.18. The DIFF field is shown in Fig. 4b and its vertical profile within the *y* domain labeled as ''PROFILE'' is presented in Fig. 5b. Within this domain, the effect of advection is negligible. The DIFF profile is positive but small at levels between the 1- and 9.5-km heights. This suggests that the bright band, although well established, is still intensifying slightly, and the stratiform precipitation rate at the surface is still increasing, presumably as a result of mesoscale uplift above the freezing level (section 3). The increase in Z_e between 0° and $-20°$C indicates that aggregation remains active. However, DIFF is strongly negative at 13 km near echo top, due to settling of hydrometeors as in the earlier period, except this settling appears to be more pronounced during this time interval.

Coincidentally, an increase in rainfall rate was recorded at many PAM (Portable Automated Mesonet) stations between 2300 and 0000 UTC (Fig. 6). Aggregation is more active when crystal habits and sizes have a broad spectrum (e.g., Sasyo 1971), which is indicative of a convective origin of the ice crystals, as suggested by Rutledge and Houze (1987). The cloud top also exhibited more pronounced sinking during this period (inferred from an increase in IR cloud-top temperature, section I.5) Thus, as the stratiform region expanded and intensified, the cloud top was sinking.

The transition from developing to mature stratiform phases is illustrated by the change in average Z_e profiles within the stratiform region from 2130–2148 to 2258–2335 UTC, displayed in Fig. 5c. Over this 100-min period, Z_e increases by over 20 dB below the 0°C level and slightly decreases above 11 km. This indicates a rapid increase of stratiform precipitation rate while the cloud top is descending. A similar evolution takes place at the trailing end of the stratiform region during a short-

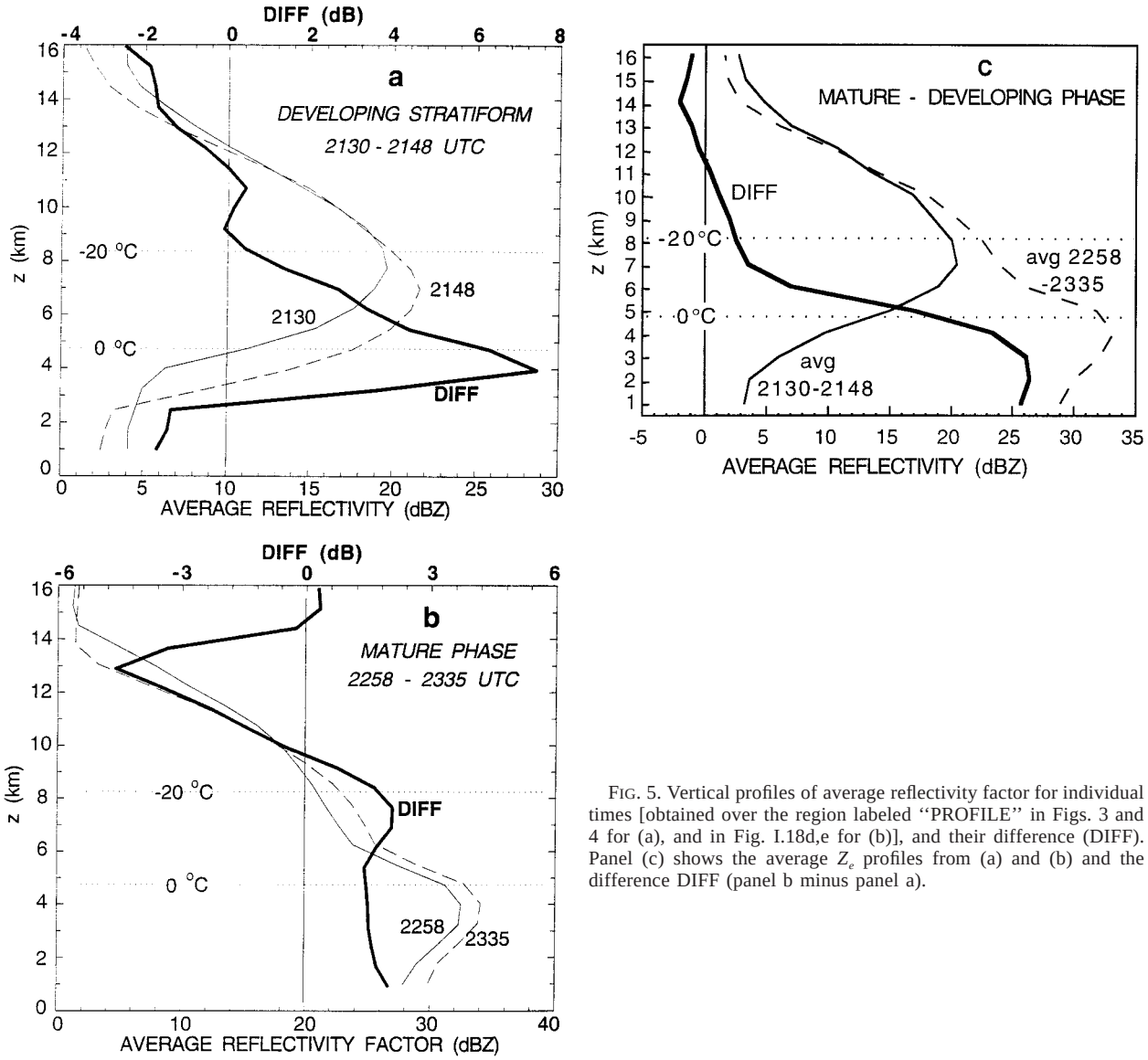

FIG. 5. Vertical profiles of average reflectivity factor for individual times [obtained over the region labeled ''PROFILE'' in Figs. 3 and 4 for (a), and in Fig. I.18d,e for (b)], and their difference (DIFF). Panel (c) shows the average Z_e profiles from (a) and (b) and the difference DIFF (panel b minus panel a).

er time span between 2258 and 2335 UTC (Fig. 4b, $5 < y < 35$); that is, the stratiform intensification is ongoing even during the ''mature'' phase. During the 2130–2148 period, negative cloud-to-ground lightning (CG, considered in part I) within this region was associated only with the trailing convection (see Fig. 1 for location). The purely stratiform region was void of CG. During the 2258–2335 UTC period, however, five positive CG emerged over the eastern portion of the stratiform region (Fig 1b), and six negative flashes occurred over the western portion in closer proximity to convective cells. These patterns further illustrate that the stratiform region positive CG are generated *after* the stratiform region achieves a mature state with significant surface precipitation.

3. Airflow profile within the stratiform region

Mesoscale wind components (u, v) and divergence (DIV) were estimated from VAD analyses (Browning and Wexler 1968). These were completed for 20 full volume scans from the CP-4 radar as the MCS evolved and moved over the radar. Because maximum elevation angles were limited to either 15° or 18.5°, the EVAD (extended VAD) technique described by Srivastava et al. (1986) was not attempted here. The VAD analysis was completed using the following parameters. (a) The primary range was 35–40 km; additional ranges of 30, 32, 37, 42, 45, and 48 km were used to fill gaps in the profile or minimize significant convective (nonlinear) perturbations. (b) The terminal fall speed (m s^{-1}) is assumed to depend only on Z_e according to

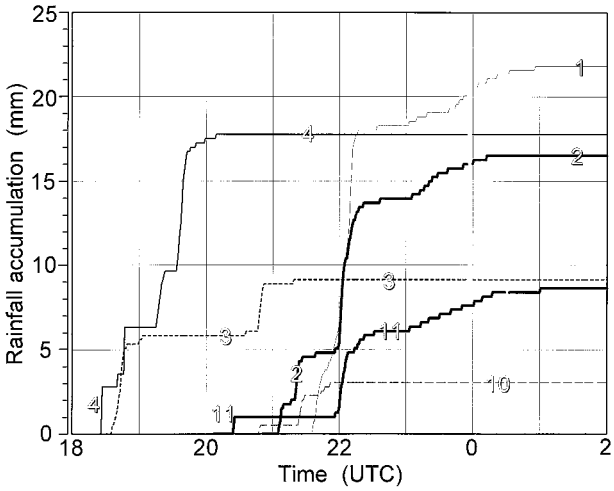

FIG. 6. Time series of accumulated rainfall from six PAM sites. The locations of PAM sites 1, 2, 4, and 11 are shown in Fig. I.2.

$$V_T = AZ_e^B \exp\left[\left(\frac{z}{10}\right)^{1/2}\right],$$

where z is height in kilometers, $A = 0.4$ and $B = 0.2$ for snow above the melting level (4.0 km AGL), and $A = 3.0$ and $B = 0.1$ for raindrops below the melting level. The correction for height z is due to the density stratification of air. (c) A 2-km filter was applied in the radial direction only. (d) Objective editing was done to eliminate points (mostly nonlinear convective perturbations) greater than 1.5 standard deviations from the best-fit linear wind field.

A final application of subjective editing (e.g., removing VAD computations from ranges that did not fit the vertical profile of u, v, and DIV) resulted in the final VAD-derived quantities, which include average Z_e, DIV, and horizontal wind. Vertical motion (w), obtained from downward integration of the DIV field, was constrained to a zero boundary condition at both the surface and cloud top, estimated from GOES IR T_b averaged over the VAD domain.

The VAD analysis assumes a linear wind field (Browning and Wexler 1968), but thunderstorm-induced flows (upper- and lower-level outflows, rotational motions) may be highly nonlinear. Using a least squares technique, a second-order harmonic (i.e., the linear wind field) is fit to the observed radial velocity V_r, which may contain small-scale nonlinear convective perturbations in V_r as in our case. When deep convection is prominent at the VAD range, the linear wind so calculated is an approximation. In order to assure adequate results, VAD plots at every elevation and range (about 2000 plots) were visually inspected. Since DIV was computed from the best-fit linear wind curve, DIV is that resulting from the estimated linear wind field. For most times, the correction for nonzero w (obtained from downward integration) at the bottom boundary was small, suggesting that the linear wind approximation was good.

Results of the VAD analyses covering the 2120–2350 time period (over the domain shown in Fig. 1) are presented in Fig. 7. The cross section represents three effects: a movement over the VAD region from the convective region to stratiform region, an evolution of stratiform precipitation, and a convective decline. A 43-min gap between 2200 and 2243 UTC, due to change in radar scanning mode, provides a separation in the analysis from a convective to stratiform ''regime'' over the region. Although the VAD domain overlaps a small portion of the averaging domain of convective line B (Fig. 1), patterns within the VAD domain will not necessarily apply to that of the convective line B domain in view of the contrasting evolution seen in each region. For example, the VAD region experienced a brief episode of intense convection near 2100 UTC (termed ''merger region'' in Figs. I.12c and I.13a), which was followed by a sudden cessation of deep convection, and the appearance of a stratiform echo. In contrast, the region of convective line B, as demonstrated in previous sections, experienced a more steady period of propagating deep convection in the form of a squall line. In short, the VAD domain contains a mix of circulations from convective line B and the more unsteady region near and east of CP-4, including the decaying remnants of cluster A (Fig. 1).

The initial portion of the VAD analysis covers the latter stages of deep convection within the VAD region. Although Z_e peaks at low levels near 2.5 km, there is no radar bright band (Fig. 7a). The fields of DIV and vertical velocity (Figs. 7e,f) are quite similar to those analyzed in the convective region of the 10–11 June 1985 squall line over Kansas (Biggerstaff and Houze 1991a). Convergence is dominant within the lower middle levels, and divergence is weakly evident at low levels and more prominent at high levels. The vertical motion profile is thus dominated by updraft, which initially exceeded 75 cm s^{-1} near the 9-km level. Such a value is appreciable in view of the large radii used in the analysis.

In the stratiform regime, a distinct bright band is apparent (Fig. 7a), and the DIV profile differs from that of the initial period. Convergence is more significant at middle levels and increases slowly with time. The mesoscale updraft–downdraft couplet observed in the stratiform region of large squall lines (e.g., Rutledge et al. (1988) is present here, although the patterns differ somewhat in relative location and magnitude. For example, the updraft–downdraft interface is located near 6–7 km, well above the melting-level location (4.7 km) where the interface more typically appears (e.g., Chong et al. 1987; Rutledge et al. 1988; Biggerstaff and Houze 1991a). The mesoscale downdraft peaks at 35–40 cm s^{-1} near 4 km and far exceeds the maximum value (<15 cm s^{-1}) of the mesoscale updraft. The mesoscale updraft magnitude ranges from very low values (<5 cm s^{-1}) at

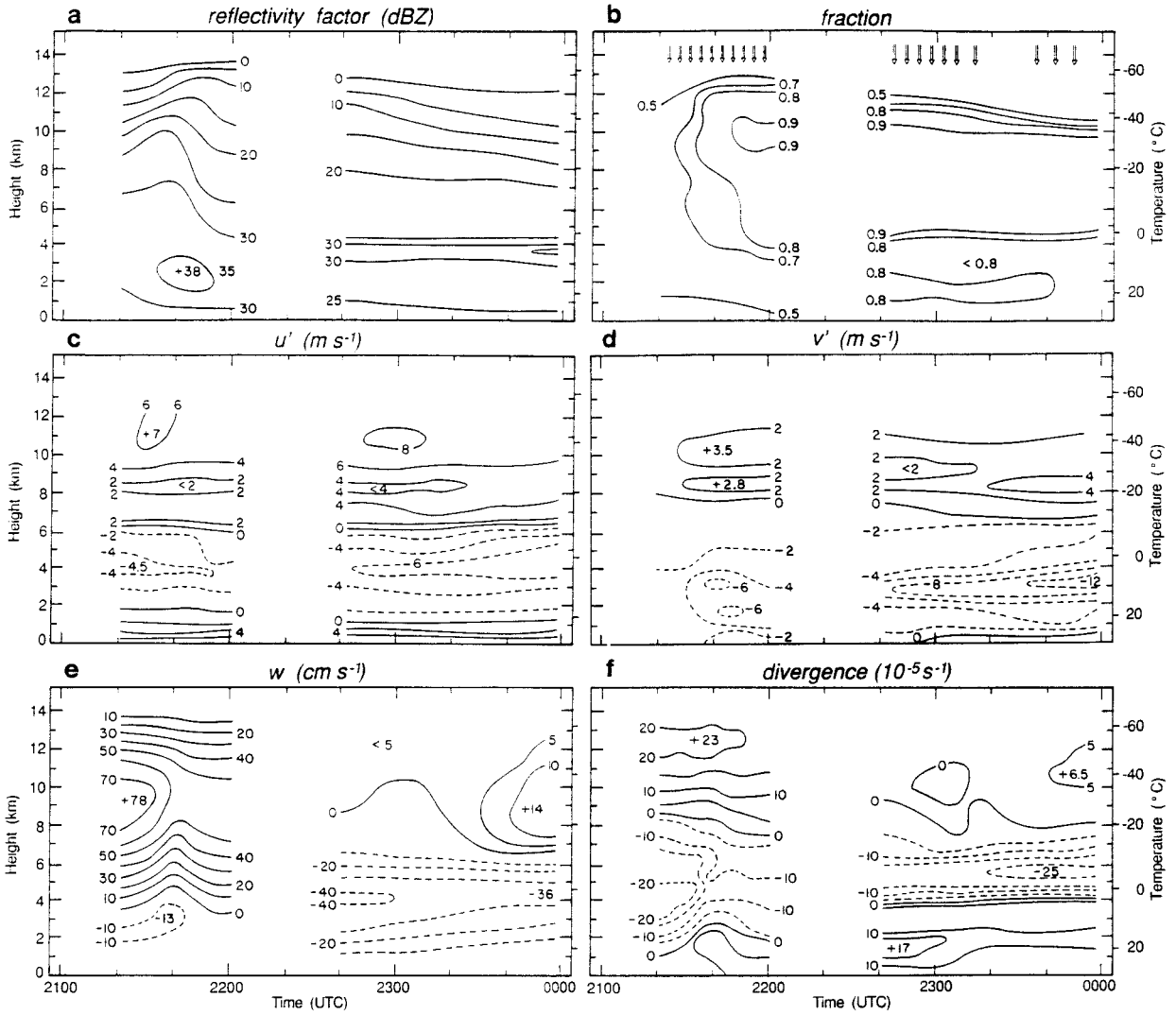

FIG. 7. Time vs height section of peak parameters obtained from the CP-4 VAD analysis over the circular domain (40-km circle) shown in Fig. 1. The arrows in (b) indicate the time of 20 individual VAD analyses, and the fraction is defined as the number of points within a given circle that have a reflectivity value greater that 0 dBZ. The horizontal velocity parameters u' and v' are departures from the base state, defined as $u' = u_{\mathrm{VAD}} - u_0$, where u_0 is the ambient zonal wind determined from the 1800 UTC rawinsonde (Fig. I.4b).

2300 UTC, increasing to approximately 14 cm s^{-1} by 2350 UTC. We are fairly confident in the apparent intensification of the mesoscale updraft at this time, because it was observed in three independent VAD analyses. It coincides with the maintenance or slight increase of stratiform precipitation from 2335 to 2350 UTC behind convective line B (Figs. I.18e,f and PAM stations 1, 2, and 11 in Fig. 6). Yet the increase may be fairly transient, and the updraft magnitude is considerably less than that observed at 2130 UTC and less than those within the stratiform region of some larger squall MCSs (e.g., Rutledge et al. 1988).

The horizontal velocity fields (u', v') displayed in Figs. 7c,d represent perturbations from the ambient values. Through its convective motions, the system appears to have rearranged the momentum field by removing excess westerly momentum at middle levels and depositing it at lower and upper levels (e.g., by vertical momentum transport and pressure forces). The perturbations in the meridional direction (v', Fig. 7d) suggest the development of a rear inflow current below an upper-tropospheric front-to-rear (southerly) flow (see section 6).

4. Cloud and precipitation structure of the stratiform region

In order to validate the VAD-derived mesoscale vertical motion, and to gain some insight in its effect on cloud-top behavior, precipitation, and vertical heat fluxes, we used the 1D bulk parameterized cloud retrieval model developed by Braun and Houze (1995, appendix

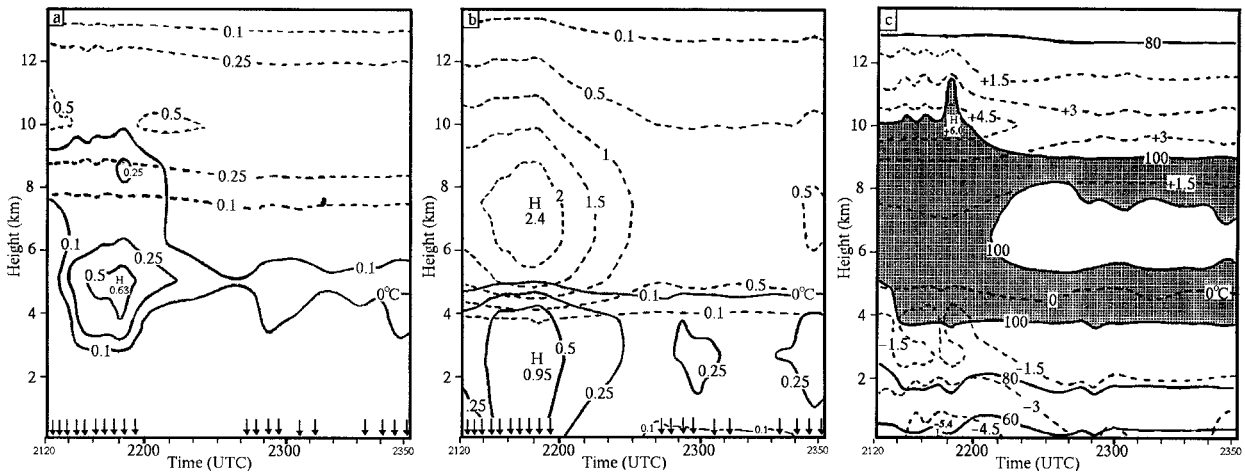

FIG. 8. Time vs height section of cloud variables in equilibrium with the VAD-derived vertical velocity profiles shown in Fig. 7e. The data gap in Fig. 7 has been filled in this analysis using cubic spline interpolation. The arrows in (a) and (b) indicate the time of individual VAD analyses. The freezing level is shown in all panels. (a) Cloud water (solid) and cloud ice (dashed), in units of grams per kilogram. (b) Rain (solid) and snow (dashed), in units of grams per kilogram. (c) Relative humidity (%, solid) and latent heating (K h^{-1}, dashed). The relative humidity (with respect to water) equals at least 100% in the shaded area.

A). A time section of these profiles is shown in Fig. 8. We note that the hydrometeor and heat flux profiles are quite sensitive to the mesoscale vertical velocity, which has its own error bars; further uncertainties arise from 1D model assumptions (appendix A), including the inability to treat horizontal advection into the VAD domain. The level of confidence is assessed using empirical relations of Rutledge and Houze (1987) to calculate Z_e from retrieved rain and snow mixing ratios (the retrieved Z_e is not shown).

In the stratiform regime, the magnitude and distribution of hydrometeor mixing ratios are consistent with previous diagnostic modeling (Rutledge and Houze 1987; Braun and Houze 1995) and in situ measurements (Willis and Heymsfield 1989), which suggests that the mesoscale vertical velocity profile is reasonably accurate. In the convective regime, the retrieved area-mean Z_e is underestimated, mainly below 0°C. This is not surprising since the VAD analysis is not highly sensitive to convective-scale vertical motion. Furthermore, since the observed Z_e is a linear average of Z_e units around the VAD column, the average Z_e is biased toward high values present during the convective regime. The retrieved Z_e, on the other hand, may be more representative of the average rain rate within the VAD column.

The retrieved maximum of approximately 28 dBZ_e at 2148 UTC at 2-km height (corresponding to the peak rain mixing ratio of 0.95 g kg^{-1} in Fig. 8b) is about 10 dB below the peak in observed area-mean Z_e located at about the same height and time (Fig. 7a). Most of the retrieved rain at this time results from melted snow because of the elevated cloud base (near 3.5 km, Fig. 8c) and weak subsidence (Fig. 7e). The underestimate of Z_e below the freezing level suggests that in reality rain formation (i.e., accretion and autoconversion) was active, which implies that in the convective regime the low-level mesoscale downdraft (Fig. 7e) is not real, as in some larger MCSs (e.g., Biggerstaff and Houze 1991a).

A second retrieved peak of about 35 dBZ_e at 2148 UTC at 7.5 km due to snow (Fig. 8a) corresponds to a ''ridge'' with nearly uniform Z_e values at this height (Fig. 7a). The VAD analysis in Fig. 7a exhibits a ridge in the Z_e field at upper levels, which occurs ahead of the peak Z_e at low levels in response to the peak mesoscale updraft at 2130 UTC (Fig. 7e). This feature is not present in the model results because by design the retrieved fields are in equilibrium with the input vertical motion.

The differences between the convective and stratiform regimes are quite striking. The stratiform regime appears to have two separate regions of cloud growth (Fig. 8c), one centered at 5-km height, which is liquid, and one at 10 km, which is frozen. Ice crystals easily fall from the upper to the lower layer without evaporating, since the intermediate layer is largely (super) saturated relative to ice. Growth of snow by riming is dominant in the lower layer. This seeder–feeder mechanism (Hobbs et al. 1980) may explain why, in the presence of weak updrafts and stronger, deeper downdrafts, the stratiform region intensified (Fig. 5b) and surface rainfall occurred (Fig. 6). The accumulated retrieved rainfall during the convective (2121–2157 UTC) and stratiform (2242–2352 UTC) regimes is 6.2 and 3.1 mm, respectively; hence, the fraction of stratiform rainfall is approximately 33%. Direct rain gauge measurements from the six sites displayed in Fig. 6 indicate a smaller stratiform fraction (based on a 5 mm h^{-1} threshold) of about 19% for the entire MCS. Figure 6 displays a clear distinction between convective (steep slope) and stratiform (shallow slope) precipitation.

Because horizontal advection is ignored, the equilib-

rium temperature perturbation has little meaning, but the latent heating, produced by the retrieved water species, can be calculated (Fig. 8c). During the convective regime, heating rates up to 6 K h^{-1} are diagnosed at 10-km height. Cooling magnitudes near the surface are similar. The level of zero heating is near the freezing level (4.7 km). During the stratiform regime, the shape of heating/cooling profile is similar but the magnitude is halved.

The observed rapid subsidence of the cloud top between 2200 and 0000 UTC (Fig. I.18) is not retrieved, simply because of the persistent upper-level updrafts (Fig. 7e), although the decrease of the snow mixing ratio at upper levels is consistent with the observed decrease in Z_e (Fig. 7a).

5. Vertical motion in the anvil

We now focus on the vertical motion near the top of the stratiform region because in section 4 we suggested that the weak upper-level updraft is at least partly responsible for the intensification of stratiform precipitation. The characteristics of ice particle habit and microphysical processes near cloud top ($T < -60$°C) are not well known in general due to limited in situ measurements. For example, ice crystal measurements within anvils of mesoscale convective systems, over the temperature range $-87°$ to -60°C (Knollenberg et al. 1993), suggest typical sizes ranging from several hundred microns near -60°C to tens of microns for temperatures less than -75°C. The magnitude of the mesoscale updraft (Fig. 7e) is uncertain because of its sensitivity to vertical boundary conditions. In particular, estimates of the cloud-top height and particle terminal velocity are required. Therefore, the estimates of ice concentrations and cloud processes by the 1D cloud model are uncertain as well. This model assumes that cloud ice does not fall out, whereas fall speeds for ice crystals of 100-μm diameter are about 10 cm s^{-1} (Heymsfield 1972), comparable to the mesoscale updraft magnitude within the upper 2 km of this MCS.

In order to refine vertical motion estimates within the anvil, and to understand the cloud-top behavior, we integrated satellite information with VAD analyses (Fig. 9). The average satellite IR brightness temperature T_b, calculated within the circle of 40-km radius used in the VAD analysis (shown in Fig. 1), shows smooth variations over a 4-h time period. The initial T_b decrease during the convective regime (signifying a rising or solidifying cloud top) is followed by a more prolonged T_b increase (downward motion of cloud top) after 2200 UTC. Although the initial cloud-top ascent from 2100 to 2200 can be related to the 50–75 cm s^{-1} mesoscale updraft diagnosed from the VAD analysis (Fig. 7e), the tendency in the subsequent cloud-top descent, which was gradual between 2200 and 2300 and more rapid after 2300 UTC, is not mirrored in weak but steady updraft (Fig. 7e) at upper levels, nor with the retrieved

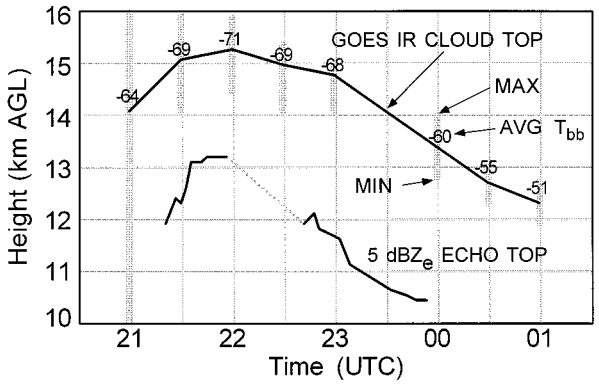

FIG. 9. Time series of GOES IR temperature averaged over the CP-4 VAD domain of 40-km radius. The bold solid line indicates the areal average brightness temperature, and the vertical bars represent the range of temperature values over the circle. The initial value at 2100 UTC shows that a portion of the domain was not covered by anvil cloud. The height estimate is based on the 2004 UTC sounding (Fig. I.4a). The thin solid line shows height of the 5-dB average Z_e contour in the VAD profiles (Fig. 7a).

evolution of cloud-top ice (Figs. 8a,b). The tendencies also disagree: the mesoscale updraft is very weak between 2240 and 2300 UTC even though cloud top descends (i.e., T_b increases) at a slow rate, while just before 0000 UTC the mesoscale updraft is more significant in the presence of a greater rate of warming at cloud top. In addition, Fig. 9 shows that in the VAD circle the average rate of subsidence of the IR cloud top between 2200 and 0100 UTC (20 cm s^{-1}) is one-half the sinking rate of the 5-dBZ_e contour between 2200 and 2352 UTC (40 cm s^{-1}). A similar observation was made for convective line B (Fig. I.18): the echo top descended 1–2 km more than the IR top between 2100 and 0000 UTC.

To reconcile these observations, we note that the average rate of subsidence of the IR cloud top between 2200 and 0100 UTC (20 cm s^{-1}) approximates the estimated ice crystal fall speed ($\sim$10 cm s^{-1}), which confirms that the mesoscale updraft is weak. The increasing discrepancy between echo top and cloud IR cloud top during development of stratiform precipitation suggests selective sedimentation; that is, the larger particles responsible for greater radar backscatter, as well as those rimed in a convective ascent, fall, while the ice concentration near the top remains sufficient to be optically thick. In particular, ice particle habits and amount of riming (and hence fall speeds) could change significantly during the transformation from convective to stratiform regimes, and hence the 10-μm emissivity could change in a manner consistent with the observations of Knollenberg et al. (1993). We suspect that even the subsidence of the IR cloud top is faster than that of the optical cloud top (which is based on some low ice concentration threshold): a reduction in ice particle concentration due to anvil spreading and selective sedimentation could lower the effective IR emission level without lowering the physical cloud top (i.e., more

IR would be upwelling from warmer levels within the anvil). In brief, we propose that weak mesoscale updrafts (10–20 cm s^{-1}) are not incongruent with cloud-top subsidence in the transformation of decaying convection into a stratiform cloud shield and that in this process typically the radar echo top subsides faster than the IR top, and the IR top faster than the visible top. A bulk parameterized cloud model cannot simulate this because it does not qualify (or nucleate) ice crystals in terms of size, habit, or amount of riming.

6. Evolution of the rear inflow jet

a. VAD and cross-sectional analyses

The outbreak of convection was followed by an increase in northerly wind mainly between 2 and 4 km (Fig. 7d). This inflow from the rear of the MCS intensified with time as the MCS moves southward. It was not the result of vertical momentum transport because the prestorm wind profile (Fig. I.4b) did not contain any northerly momentum relative to the flow at the 2–4-km height. In a storm-relative sense (the storm motion is defined in Fig. I.4b), this is a rear-to-front inflow, with a peak magnitude of 3 m s^{-1} at 2140 UTC increasing to 9 m s^{-1} at 2350 UTC. An RHI (range–height indicator) at 2006 UTC through cluster A (Fig. I.17) shows that a rear inflow jet was also present in the early development stage of the trailing stratiform region of cluster A (Fig. 1a), prior to the development of the squall convective line B and its more extensive stratiform region, and nearly 1 h before the time of maximum convective activity (section I.4b). The jet was fully developed 2.5 h after the very first echoes associated with cluster A appeared. This timing is in agreement with numerical simulations by Weisman (1992). The early presence of the jet is also in accordance with observations of a North Dakota MCS (Klimowksi 1994) in which a rear inflow jet was observed 20 min after squall line formation. The maximum ground-relative speed within this jet is 15 m s^{-1} toward 160°. This subsiding jet appears to connect with the upper convergent portion of the convective-scale downdraft near the 2–3 km AGL.

In the mature stratiform phase, the rear inflow jet is located just below the freezing level and at the level of maximum mesoscale subsidence (Fig. 7e). This indicates that the apparent slight rise of the jet within the VAD circle between 2250 and 2350 UTC is a spatial rather than a temporal change; that is, the rear inflow jet subsides as it penetrates the stratiform region, as is the case in some larger squall MCSs (e.g., Smull and Houze 1987; Biggerstaff and Houze 1991a).

It is uncertain from the VAD sequence whether the apparent strengthening in time of this rear inflow jet is due to actual evolution rather than to spatial differences. In a Great Plains squall line, Klimowski (1994) finds that the rear inflow develops very early in the rear of the squall line and expands rearward as the stratiform region develops. As convection dissipates, the rear inflow also decays, first at the leading edge and later toward the rear.

This question is clarified through inspection of vertical north–south sections passing through CP-4. These sections were obtained via interpolation of volume scan data (the same as used in the VAD analyses) to a 3D grid and then forming vertical cuts in the north–south direction through the CP-4 radar location. Figure 10 presents fields of Z_e and V_r. The sign of V_r is such that it corresponds to v, the meridional wind component, but the velocity is not corrected for the hydrometeor fall speed contributions. In the radar blind cone, Fig. 10 shows individual profiles of Z_e and w taken from the VAD analyses. At 2130 UTC deep convective elements are merging very near CP-4, and significant upward motion is indicated. Cells located near $y = -75$ (Fig. 10a) are associated with the north–south convective line C shown in Fig. 1a. Significant outflow at higher levels exists within the anvil both north and south of CP-4.

Within the anvil region north of CP-4, the developing rear inflow jet exhibits a peak ground-relative speed of about 13 m s^{-1} in a storm-relative frame), similar to estimates from VADs and RHIs. This jet subsides toward the convective region and its leading edge moves southward with time (Figs. 10c,d), to coincide with the southward-moving convective line (Figs. 10e,f). These sections clearly show that the apparent lifting of the rear inflow (Fig. 7d) with time is due to the slope of the rear inflow jet and the southward displacement of the MCS. While convective activity atrophies (as evidenced by the weakening of the mesoscale updraft, the Z_e values in the convective cores, and the divergence aloft), the rear inflow jet retains its strength and protrudes well into the MCS by 2350 UTC. In individual RHI sections, such as shown in Fig. 11, the rear inflow jet is well defined. Figure 11 indicates a veering (from 3 h earlier) of the inflow jet maximum, consistent with Coriolis forcing. At both 2258 and 2350 UTC this jet enters the system near the 7-km AGL level at $y = 75$ and gradually descends to low levels near the convective line, with speeds accelerating to 12 m s^{-1}.

The height and strength of the VAD-derived downdraft shown in the profiles of Figs. 10d and 10f are consistent with this descending current. Because the snapshots at 2258 and 2350 UTC in Figs. 10d and 10f are very similar, they approximate a steady state. Therefore, we can picture the rear inflow jet as a material entity through which air parcels flow. Then the mean storm-relative rear inflow of 5 m s^{-1} implies a subsidence of 18 cm s^{-1}, which compares well with the mean VAD-derived downdraft between 1 and 6 km AGL. Additional evidence of this subsidence is given by the drop in equivalent potential temperature θ_e at the surface within the study area from 355 to 360 K at 1900 UTC to about 338 K after 2200 UTC (Fig. I.10). In the 1800 and 2004 UTC soundings, θ_e exceeded 338 K at all

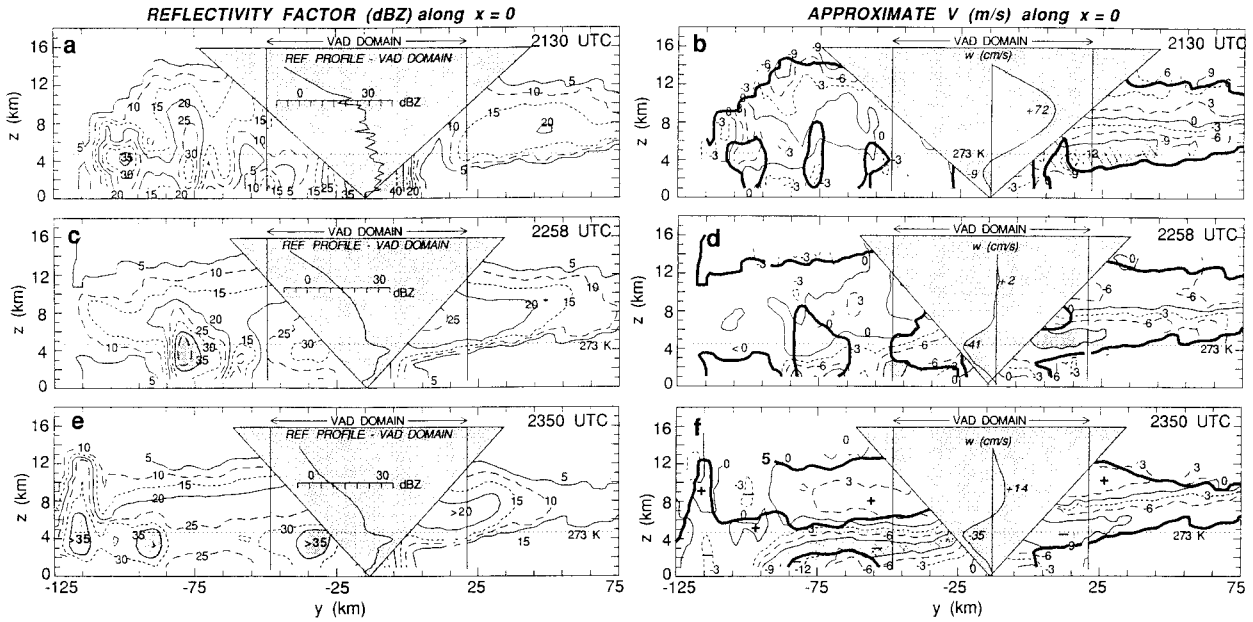

FIG. 10. Vertical sections of Z_e (left panels, contoured every 5 dB beginning at 5 dBZ) and approximate meridional velocity v, derived from radial velocity (right panels, contoured every 3 m s^{-1}) within the north–south vertical plane passing through CP-4. The location of the cross sections is shown in Fig. 1 as the line along $x = 0$. Vertical profiles of Z_e and vertical velocity w, obtained from the VAD analysis (Figs. 7a,e), are superimposed on the respective cross sections of Z_e and v. The bold lines in the right panels represents the 5- and 25-dBZ_e reflectivity contours. The shaded area represents $v < -6$ m s^{-1}, that is, the region of rear inflow.

levels, except between 3.4 and 5.1 km. Therefore a large amount of air from this level must have been transported and/or entrained down to the ABL. Simultaneous with the development of the rear inflow jet, a weaker, slowly ascending front-to-rear flow develops above this jet (Fig. 10f). This flow pattern is similar to that through convective line B, which we consider next.

b. Composite radial velocity analysis through convective line B

In Fig. 12 the evolution of the V_r field averaged over a limited 20-km east–west domain ($-60 < x < -40$, Fig. 1) is presented. The azimuth of view is shown to aid mental conversion to Cartesian components; for example, negative V_r values near 270° azimuth indicate westerly wind. The V_r patterns reveal an airflow structure within convective line B that is distinctly unsteady, as are the corresponding Z_e fields (Fig. I.18). At 2057 UTC, a westerly flow that peaks at 2 km AGL is capped by a weaker easterly flow ($V_r > 0$) above $z = 10$ km. This pattern corresponds with the 2004 UTC sounding (Fig. I.4b). By 2157 UTC, a westerly jet ($V_r = 14$ m s^{-1}) emerges at middle levels within the convective region near $(y, z) = (-25, 7)$. These patterns indicate that locally the flow along the line is greater in magnitude than flow perpendicular to it. One hour later (2258 UTC) this same westerly or southwesterly jet can still be seen, although it is broader, and a new jet (containing northerly and/or westerly flow) is centered near $(y, z) = (25, 6)$ within the expanding stratiform region. This latter feature is believed to be the rear inflow jet, which was well developed by this time (Fig. 7d). The flow at low levels within the convective line (near $y = -60$ in Fig. 11c) is either northerly or easterly, and its northerly component may be a continuation of the rear inflow jet into the convective line, similar to the RHI in Fig. 11. The same continuous, subsiding jet appears to be present at 2350 UTC (Fig. 12d).

Easterly flow continues at higher levels south of the convective region. The V_r pattern at 2157–2258 UTC

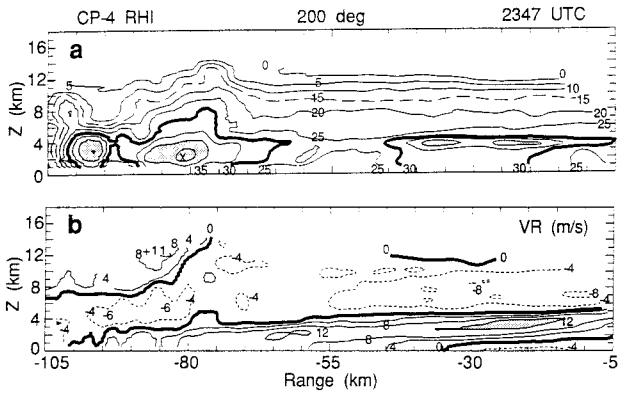

FIG. 11. CP-4 RHI at 2347 UTC toward 200°, intersecting the remnants of convective line B and part of the trailing stratiform region. The location of this profile is shown in Fig. 1c. (a) Equivalent reflectivity factor Z_e, contoured every 5 dB beginning at 0 dBZ_e. Areas with $Z_e > 40$ dBZ_e are shaded. (b) Radial velocity V_r, contoured every 4 m s^{-1}. The bold line is $V_r = 0$. The shaded region ($V_r > 12$ m s^{-1}) highlights the rear inflow jet.

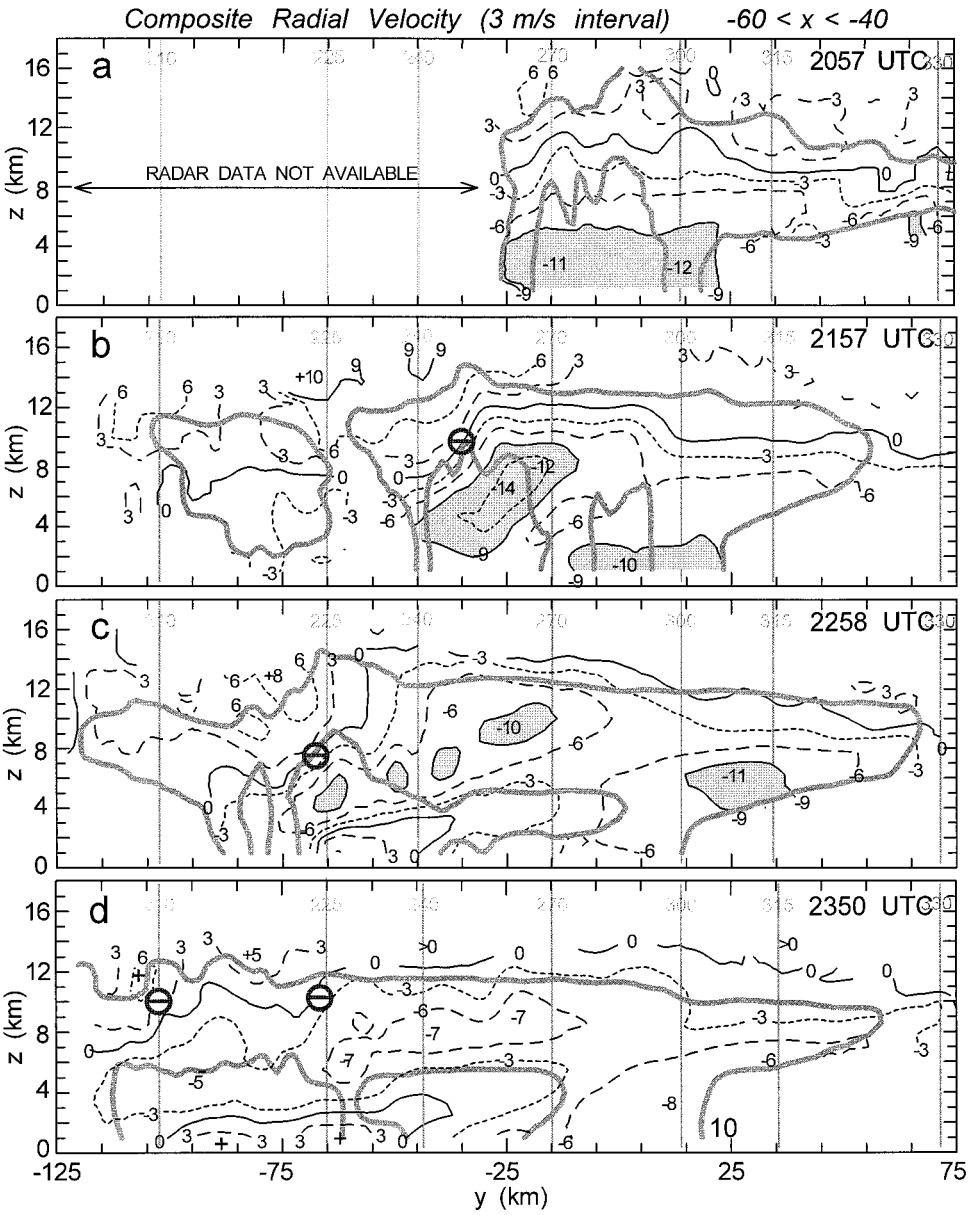

FIG. 12. Analyses of radial velocity within convective line B, averaged over the east–west domain $-60 < x < -40$ indicated in Fig. 1. Negative values are approaching flow. The contour interval is 3 m s^{-1}. The circled "−" symbols indicate significant anticyclonic shear mentioned in the text. The bold solid lines in panels (a)–(d) are Z_e contours of 10 and 25 dBZ_e, transposed from Figs. I.18a,c,d,f, respectively. The CP-4 azimuth angle evaluated at $y = -50$ is shown above each panel.

(Figs. 12b,c) suggests the development of a negative vertical vorticity within the convective region between 4 and 14 km peaking near -10^{-3} s^{-1} at $z = 10$ km. This negative vorticity weakens as convection decays after 2157 UTC. It weakens first at middle levels and later at upper levels, and during this process it moves rearward toward the stratiform region. Biggerstaff and Houze (1991b) find a core of positive vorticity at mid-levels in the convective part of the 10–11 June 1995 mature squall line with trailing precipitation.

The presence of southerly/westerly flow above the decaying convection [-5 m s^{-1} at $(y, z) = (-95, 5)$] at 2350 UTC (Fig. 12d) and northerly/westerly flow to the rear [-6 m s^{-1} at $(y, z) = (35, 6)$] suggests a broad belt of front-to-rear flow ascending over subsiding rear-to-front flow, respectively. Comparison of flow magnitudes at this time show that all flows weakened with time and tended toward horizontal stratification as the system entered the dissipating stage. Such a decline closely paralleled that seen in Z_e and illustrates that this

MCS was distinctly unsteady from both microphysical and kinematic viewpoints.

In summary, the above analyses reveal a rear inflow jet quite similar to that found in larger squall-line systems that exist in higher-shear environments (Smull and Houze 1987a). This sequence of airflow cross sections further shows that the rear inflow jet is present at the time of most intense convective activity (as in the study by Klimowski 1994), and the jet accelerates slightly as it descends and approaches the convective line [in agreement with the theory of Lafore and Moncrieff (1989)]. In contrast with Klimowski (1994), the jet does not decay in tandem with the waning on convective activity, rather it remains prominent and becomes the dominant flow feature in the mature MCS.

7. Mesoscale flow and vorticity

Numerical simulations of deep convection (e.g., Rotunno et al. 1988; Weisman 1992) indicate that the metamorphosis of unorganized convection to a single MCS, and the longevity of an MCS, critically depend on the low-level ambient wind shear. However, the definition of the ambient flow becomes difficult (Brooks and Doswell 1994) as convective clusters and lines develop and in turn impact the low-level flow. A knowledge of the evolution of the mesoscale flow during the development of this MCS may give some insight into why some lines or clusters merged into a single squall line at the mature stage, and others decayed. Another question concerns the mesoscale effect of the intensifying rear inflow jet discussed in section 6. A third, related question is whether a midlevel MCV developed during the short lifetime of this small MCS.

Our interest is primarily on the MCS-wide scale; since the various Doppler radars (Fig. I.2) were positioned such as to synthesize convective-scale flow, not mesoscale flow, multiple-Doppler analyses were not possible on the MCS scale. There are various techniques to estimate the full 2D horizontal flow by means of a single radar (Shapiro et al. 1996). They all assume a Lagrangian conservation of Z_e as a means of estimating the horizontal velocity component normal to the radial velocity. While this is a bold assumption, we assume here that the horizontal motion of finescale Z_e structures approximates the horizontal wind with sufficient accuracy to recover important features of the mesoscale flow. In this MCS the horizontal and vertical flow fields appear to be changing faster than the Z_e field, and the vertical shear of horizontal wind was rather small. We demonstrate below, with internal consistency checks and comparison with radial velocity data, that the mesoscale flow field is retrieved reasonably well for our case.

We used two methods. One is a pattern correlation technique called TREC [tracking radar echoes by correlation; Tuttle and Foote (1990)], which estimates the mesoscale flow by tracking radar echoes in successive scans (appendix B). This technique was developed initially to describe the mesoscale flow in the presence of convective storms, by means of a single (Doppler) radar (Rinehart 1979), but has since been used to estimate the ABL flow (Tuttle and Foote 1990). We used TREC because other techniques of single-Doppler velocity retrieval are more cumbersome and cover a smaller domain.

A second technique uses the VAD-derived velocities and its kinematic components (Figs. 7c,d) to estimate the profile of vertical vorticity that best approximates the observed movement of echo patterns within the VAD circle (Lu et al. 1996).

a. Storm-relative mesoscale motions

The evolution of the mesoscale flow field obtained from TREC at altitudes of 2 and 8 km is shown in Fig. 13. The flow pattern generally corresponds well with ambient flow profile as measured by radiosonde (appendix B), yet locally significant departures occur. For instance, significant convergence is present aloft in the trailing region of convective line C (Fig. 13d), which is consistent with the lack of developing region of stratiform rainfall behind C. The negative vertical vorticity apparent in the single-Doppler fields near the leading edge of convective region at 2157–2258 UTC (Figs. 12b,c), mainly at $z = 10$ km, are corroborated in the TREC analysis (2245 UTC at 8 km, Fig. 13f, at $-60 < x < -40$ and $y = -65$). At 2 km, a rear inflow (northerly) current is absent at 1926 UTC (Fig. 13a), but it appears at the northern fringe of the MCS at 2104 UTC (Fig. 13c) and it is well established by 2245 UTC (Fig. 13e).

The vertical structure of the storm-relative meridional flow at the time of development of the stratiform region is shown in Fig. 14, which displays an average over the same domain as the Z_e field ($-90 < x < -20$, Fig. 1). The TREC analysis clearly shows the rear inflow current underneath an ascending front-to-rear flow. The mesoscale vertical motion field shown in Fig. 14 is derived from the TREC winds, and a variational method was used to impose a second (top) boundary condition on the upward integration of the mass continuity equation. The bottom boundary was at the surface, using convergence values at 1 km AGL, and the top boundary at 11 km, using the convergence field at 10 km. The top boundary is 2–3 km below the echo top. Notwithstanding the indirect wind estimates and the many assumptions involved, the location of the main updraft corresponds well with the convective core of convective line B. There is even an upper-level mesoscale updraft and lower-level mesoscale downdraft within the stratiform region. The magnitudes of these drafts are similar to that derived from the VAD analysis at this time (Fig. 7e), but the updraft ($+24$ cm s^{-1} at a height of 8 km) is stronger than the downdraft (-5 cm s^{-1} at 3 km).

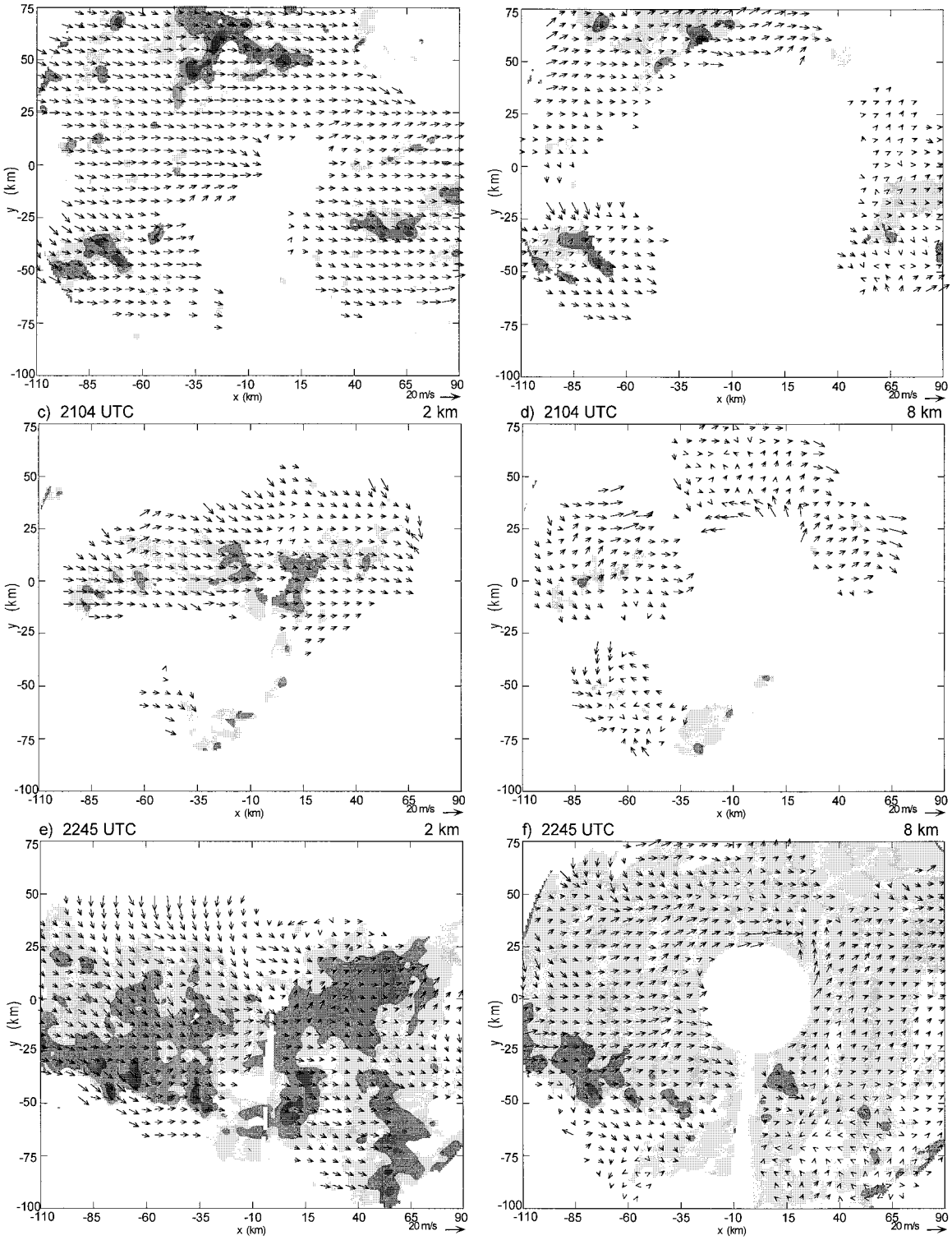

FIG. 13. Mesoscale flow vector field estimated with the TREC technique, and contours of Z_e at three levels (10, 25, and 40 dBZ). Two heights are shown, 8 (top) and 2 km (bottom), as well as three times, 1924 (a)–(b), 2104 (c)–(d), and 2243 UTC (e)–(f). The time given marks the beginning of the first of two successive volumes of radar data. The CP-4 radar is at the origin of the grid.

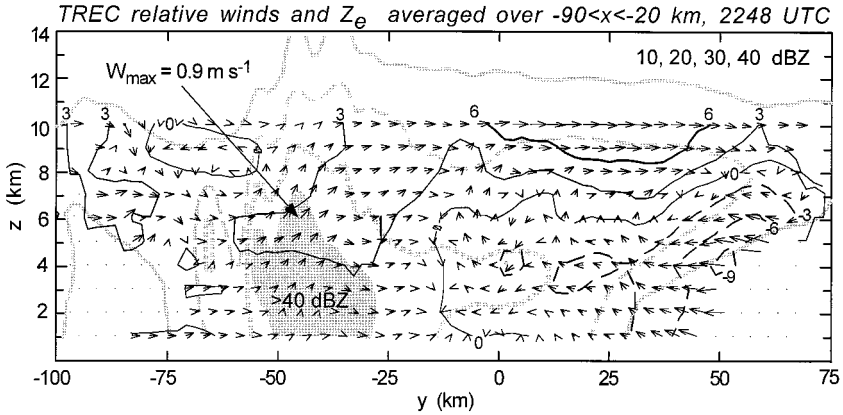

FIG. 14. Meridional cross section of average Z_e and storm-relative, TREC-derived airflow through the MCS at 2250 UTC. The averaging domain is the same as that for Z_e in Fig. 1. The Z_e contours are thick gray lines, with $Z_e > 40$ dBZ$_e$ shaded. Storm-relative flow is contoured as black thin lines, contoured every 3 m s^{-1}. Solid contours are positive (front-to-rear flow) and dashed contours are negative (rear inflow). The location of the maximum averaged upward motion is shown.

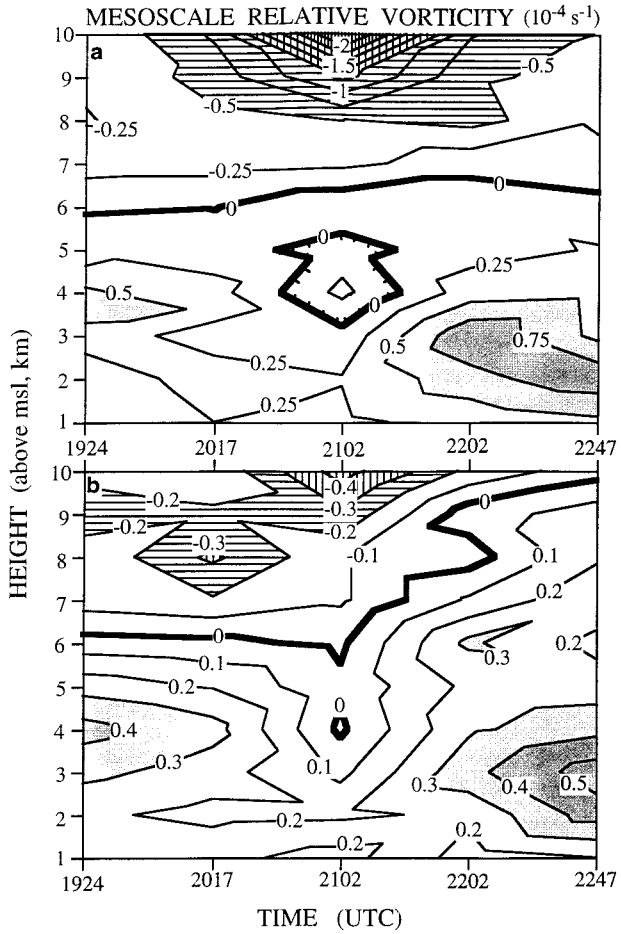

FIG. 15. Time–height sections of the mesoscale vertical vorticity (10^{-4} s^{-1}), as estimated by means of (a) the TREC technique; and (b) the method of Lu et al. (1996). The zero line is bold, and areas of significant cyclonic (anticyclonic) vorticity are shaded (hatched).

b. Mesoscale relative vorticity

GOES visible imagery revealed a mesoscale cyclonic vortex in a neighboring, unrelated MCS. This MCS formed in western Kentucky around 0000 UTC 13 July and dissipated over central northern Tennessee around 1700 UTC (labeled ''MCS remnant'' in Fig. I.5a). While a clear midlevel MCV of the kind described by Brandes (1990) did not develop in the stratiform region of the MCS in our case, further analysis of the TREC mesoscale winds did reveal the presence of weak cyclonic vorticity at middle levels. Cyclonic vorticity was also observed directly on smaller scales, from the cell updraft scale (~2–5 km) upward to the cloud scale of about 10 km. For example, a pronounced cyclonic rotation of approximately 10-km scale (labeled as ''CYC'' in Fig. 1a) was observed at middle levels in association with the dissipation of intense but transient convective elements near CP-4 after 2100 UTC.

The evolution of the systemwide vertical vorticity at various levels is summarized in Fig. 15. In Fig. 15a the TREC-derived relative vorticity is averaged over all data points in the entire domain of Fig. 13. The relative vorticity values in Fig. 15b are those that produce, within the VAD circle, the horizontal flow field that produces the best (semi-Lagrangian) advection of radar reflectivity, in a least squares sense. By definition, a linear horizontal flow field can be fully described by translation, divergence, deformation, and vorticity. The first three components are derived from the VAD analyses (Fig. 7), and the vorticity is unknown. A basic assumption (and the same as that used in TREC) of this iterative technique (Lu et al. 1996) is that the reflectivity within the VAD circles is conserved from one radar volume to the next. The two results are expected to vary not just because they are based on different techniques, but also because the domain differs.

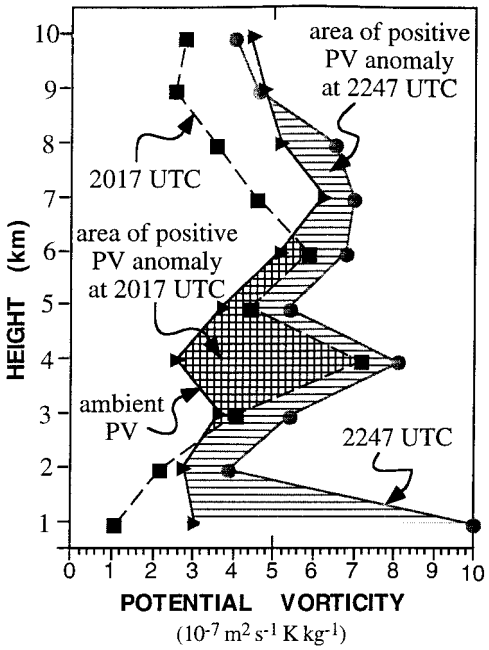

FIG. 16. Vertical profiles of potential vorticity. The profile at 2017 UTC is derived from the 2004 UTC MSFC sounding (Fig. I.4a) and the average of the relative vorticity profiles at 2017 UTC in Figs. 15a and 15b. The profile at 2247 UTC is derived from a convectively mixed sounding (evaluated as 30% 2004 UTC MSFC sounding and 70% pseudoadiabatic sounding, shown by the dashed curve in Fig. I.4a) and the average of the relative vorticity profiles at 2247 UTC in Figs. 15a,b. The ''ambient'' profile represents the preconvective environmental conditions and is derived from the 1200 UTC analysis of the synoptic net of rawinsonde data. Relative vorticity is evaluated in height coordinates for the 2017 and 2247 UTC profiles, and in isentropic coordinates for the ambient profile.

Figures 15a and 15b have the following characteristics in common.

- The maximum values of mesoscale vorticity in this MCS are close to the Coriolis parameter.
- Cyclonic vorticity is generally found below a height of 6–7 km, that is, coincident with the mesoscale downdraft region (section 5), and anticyclonic rotation above this height.
- Cyclonic vorticity appears to increase as the MCS evolves into a mainly stratiform system.

In general, the magnitude of the vorticity values estimated by the Lu et al. method is smaller than that derived from TREC winds, even though the VAD circles are smaller than the TREC domain. It is not clear why this is the case. Also, the TREC technique produces very large negative vorticity values that occur aloft mainly at 2102 UTC, with a spike of -2.6×10^{-4} s^{-1}. The existence of anticyclonic vorticity is confirmed by Fig. 15b and other independent data points near the height and time of this spike in Fig. 15a, but the large magnitude is an artifact due to low biases in Z_e associated with CP-4 transmitter problems during the 2102 volume scan (this area can be seen in Fig. 13d, at $x = 15$ and $y = 25$). A third major difference is establishment of weak cyclonic vorticity above the 6-km height after 2102 UTC in the Lu et al. technique. The TREC method generally performs worse than other techniques at this stage of stratiform expansion, but both methods become unreliable after 2247 UTC because there simply are not enough clearly identifiable echoes within the uniform stratiform region.

c. Mesoscale potential vorticity

A well-defined midlevel MCV and associated echo signature did not develop in this MCS. The mesoscale flow field suggests that net cyclonic vorticity was present below 6 km and anticyclonic vorticity aloft. Raymond and Jiang (1990) postulate that mature MCSs contain a negative potential vorticity (PV) anomaly near the tropopause and a low- to middle-level positive PV anomaly, on account of the deepening and stabilization of the troposphere by convective motions, respectively, and that this PV anomaly profile can interact with the low-level shear to induce further lifting and thus enhance the longevity of some MCSs. We examine the PV profile in our case study and use Rossby's approximation of PV:

$$P = -g(\zeta_\theta + f)\frac{\partial \theta}{\partial p}, \tag{1}$$

where g is gravity, ζ_θ the relative vorticity on an isentropic surface, f the Coriolis parameter, θ the potential temperature, and p the air pressure. We define the base PV as that present in the synoptic environment and the PV anomalies as mesoscale departures from this base PV (Fig. 16). In the early stages of this MCS we find a negative PV anomaly near the surface and above a height of 6 km. A positive PV anomaly exists between the 3- and 6-km heights. The algorithms of mesoscale velocity retrieval we used are not suited for the anvil region above 10 km, so the PV anomaly there is unknown. As the MCS matures between 2017 and 2247 UTC, PV increases at all levels, especially near the surface and between 6 and 10 km, and the PV is anomalously positive from the surface to 9 km. This increase is due to a combination of stabilization by convective motions and increase in relative vorticity (Fig. 15). These observations confirm the starting point of the theory of Raymond and Jiang (1990), that is, that an MCS has an upper-level negative PV anomaly and a positive PV anomaly in the lower troposphere.

The increase in PV during the intense convective activity between 2017 and 2247 UTC is largely due to latent heat release. In particular, a dipole of diabatic cooling in the lower troposphere and diabatic heating aloft increases midlevel PV. According to Bluestein [1993, Eq. (1.9.48), p. 217]

$$\frac{1}{P}\frac{DP}{Dt} \approx \frac{\partial}{\partial \theta}\left(\frac{D\theta}{Dt}\right), \tag{2}$$

where D/Dt is the total or material derivative. The equation is only approximate, since it ignores the terms due to friction and horizontal absolute vorticity. A scaling argument shows that these terms are significant only near the ground and near the perimeter of the MCS. In this case, there is a vertical gradient of latent heating of up to 10 K h^{-1} between the surface and 10 km (or between $\theta = 300$ K and $\theta = 345$ K) (Fig. 8c). In other words, if the high latent heating rates would be maintained, PV would increase exponentially at an *e*-folding time of 4.5 h. From 2017 to 2247 UTC, the PV between 1 and 10 km is estimated to increase by 60% on average (Fig. 16). This increase corresponds with an *e*-folding time of 5.3 h; that is, the growth rate of PV appears to be well explained by latent heating alone. In addition, PV increases more rapidly at levels where the vertical gradient of latent heating is high (near the surface and between 7 and 9 km). These back-of-the-envelope calculations confirm our estimates of distributions of latent heating and potential vorticity, and the basic dynamics of this MCS. As the MCS decays, it is expected to leave behind a mesoscale positive PV signature, since PV is conserved in the absence of diabatic or dissipative effects. It remains an open question how long lived such residual PV anomaly blobs are and how, if at all, the PV blobs resulting from the various MCSs that formed around this time interacted.

8. Summary and conclusions

This paper documents the evolution of the mesoscale flow and precipitation within a relatively small MCS that formed in a weakly sheared environment. We have focused on (a) how this mesoscale organization takes place, in particular how the stratiform region develops; (b) how the rear inflow current evolves; and (c) whether a mesoscale cyclonic vortex forms. In consideration of the findings of Rotunno et al. (1988), the lack of environmental shear is likely the most important factor behind the relatively rapid collapse of this MCS after it had attained the archetypal structure of a leading convective line and a trailing stratiform region.

Detailed radar observations reveal the rapid development of a stratiform precipitation region to the rear of the convective line, within a prominent mesoscale updraft of 50–70 cm s^{-1} magnitude, 4 h after first echo. The stratiform region expanded rearward and intensified, as evidenced by an in situ increase in Z_e primarily below 10 km, and is most significant near the bright band. Some of this precipitation growth appears to have been generated within the stratiform region as convective elements dissipated in a time-dependent fashion [in a manner similar to the particle fountain concept advanced by Yuter and Houze (1995c)], as opposed to being transported directly from the region of active deep convection. As the stratiform region further evolved to a 50–100-km-wide structure exhibiting a prominent bright band, the cloud top descended, slowly in terms of IR brightness temperature ($\sim$0.2 m s^{-1}) and more rapidly in terms of Z_e, notwithstanding a weak but sustained mesoscale updraft within the anvil.

VAD analyses of vertical motion showed a dominance of initial deep mesoscale updraft (and rising cloud top) associated with intensification and expansion of stratiform precipitation. A variable pattern in very weak (5–15 cm s^{-1}) mesoscale updraft activity at upper levels and a more pronounced mesoscale downdraft (30–40 cm s^{-1}) was present during the mature stage. The mesoscale downdraft was deeper in this case (6.5 km—extending 2 km above the melting level) than in most other documented cases.

The radial velocity pattern in series of RHI and averaged cross sections, as well as the VAD and TREC analyses, demonstrate the presence of a well-defined, slowly subsiding rear inflow current, quite similar to that found in larger squall line systems that exist in higher-shear environments (Smull and Houze 1987a). A broader and weaker ascending front-to-rear current developed above the rear inflow jet. The rear inflow jet formed early, 2.5 h after first echo [in accordance with simulations by Weisman (1992)] and 1 h prior to the time of most intense convective activity (as in the study by Klimowski 1994). The jet accelerates slightly as it descends and approaches the convective line or its remnants, in agreement with the theory of Lafore and Moncrieff (1989). It is a persistent feature in the cross sections, and its altitude and strength are consistent with the VAD-derived mesoscale downdrafts. In contrast with Klimowski (1994), the jet did not decay in tandem with the waning of convective activity; rather, it became the dominant flow feature as the MCS entered its dissipating stage.

The mesoscale flow field was estimated within the developing MCS by means of the TREC technique. Unlike dual-Doppler analysis, this technique samples the entire MCS but becomes unreliable when the echoes are very transient or when the precipitation is stratiform. A well-defined midlevel mesoscale cyclonic vortex did not form as the MCS matured, but the profile of mesoscale vertical vorticity, estimated by means of the TREC method, as well as by a semi-Lagrangian advection technique within the VAD circles (Lu et al. 1996), appears to have been cyclonic below 6–7 km and anticyclonic aloft. A positive potential vorticity anomaly existed at midlevels (3–6 km) within the MCS, and potential vorticity increased in strength and in depth during the development of the MCS. This increase is consistent with the estimated vertical distribution of latent heating.

One fascinating aspect of this case study is similarity of kinematic and precipitation characteristics between this small MCS and larger, longer-lived systems, which suggests that the dynamical and microphysical mechanisms of mesoscale organization are similar for a wide range of MCS horizontal dimensions. This similarity evokes the question of whether there is a preferred scale for an MCS, and whether this scale dependency is a

function of ambient stability and wind shear. This study does demonstrate that a small, unsteady MCS, developing in an environment with moderately large convective available potential energy and very weak shear, which is insufficient to support a long-lived system, may assume essentially the same cloud, precipitation, and airflow characteristics as larger, long-lived MCSs. This suggests that these characteristics are inherent to MCSs and that the MCS size and longevity above certain thresholds are largely irrelevant.

Acknowledgments. We gratefully acknowledge Dr. S. Braun for providing the University of Washington 1D cloud-microphysical model and Dr. Y. Y. Lu for making available his Lagrangian advection scheme. This research was sponsored by NASA under Grant NAG8-654 and by NSF under Grants ATM-8800606 and ATM-9200667. The National Center for Atmospheric Research (also funded by NSF) provided computing resources and software (RDSS, REORDER, CEDRIC, and VAD analysis) used in this study.

APPENDIX A

Estimation of the Equilibrium Cloud and Precipitation Structure

The cloud microphysical variables shown in Fig. 8 are derived from a one-dimensional bulk-parameterized retrieval model by Braun and Houze (1995). This model uses a temperature and humidity profile (we use the MSFC sounding at 2004 UTC, Fig. I.4a) together with an area-mean vertical velocity profile (here the VAD derived vertical velocity profiles shown in Fig. 7e) to estimate the profile of liquid and frozen cloud and hydrometeor mixing ratios. The retrieved mixing ratios represent average conditions within the VAD domain for both stratiform and convective precipitation under the following assumptions: (a) the observed airflow is sufficiently steady to obtain a balanced cloud and precipitation response; (b) the area-mean microphysical source terms are the same as the source terms based on area-mean mixing ratios; (c) the fraction of the area-mean mixing ratio (r_a) to the perimeter-averaged mixing ratio (r_p), r_a/r_p, is known for all water species.

The rather slow changes of the vertical velocity in time both in the convective and the stratiform regimes (Fig. 7e) suggest that the first condition (a) is valid. Sensitivity tests by Braun and Houze (1995) suggest that (b) is true. The fraction r_a/r_p can be estimated at any time from the reflectivity within and along the VAD circles (shown in Fig. 1), at least for rain and snow. For cloud ice, we assume that $r_a/r_p = 1$ in the convective regime and $r_a/r_p = 0.9$ in the stratiform regime.

Some other parameters used for the retrieval model are shown in Table A1. In the convective regime snow has graupel-like characteristics, while in the stratiform regime it represents dendritic crystals. The number of iterations required for the 20 profiles shown in Fig. 8 was typically near 100 but varied between 50 and 300.

TABLE A1. Parameters used in the one-dimensional retrieval model. The fall speed of snow (V, m s^{-1} is calculated as $V = aD^b$, where D (m) is the diameter and a and b are given in the table.

	Convective regime (before 2200 UTC)	Stratiform regime (after 2230 UTC)
Eddy diffusivity (m^2 s^{-1})	2000	1500
Density of snow (kg m^{-3})	230	150
Coefficient for snow (a)	12.4	247
Exponent for snow (b)	0.42	0.82

APPENDIX B

TREC Analysis

The TREC (tracking radar echoes by correlation) analysis was performed on a series of sequential pairs of CP-4 scan volumes in the radar spherical coordinate system. Time separation between volumes was 3–5 min. A number of editing steps was taken to remove ground clutter, data spikes, and vectors whose radial component differed from the measured Doppler velocity by more than 5 m s^{-1} [see Tuttle and Foote (1990) for details]. Then each set of constant elevation angle vectors was interpolated to a two-dimensional Cartesian grid on the fixed elevation angle surfaces using a least squares method. This was followed by a simple linear interpolation in the vertical direction to obtain the vectors on constant altitude planes, from 1 to 10 km in 1-km increments. The vector field was patched and filtered using a two-step horizontal Leise filter 4Δ (Leise 1981), where $\Delta = 1$ km is the grid spacing. The result is the vector field in Fig. 13. The number of elevation angles used varied between 5 and 9; the highest elevation angle was 12°. Therefore there are no TREC velocities near the origin at a height of 8 km (Figs. 13a,c,e).

In recent work by one of the authors (JLT), TREC has been applied to a variety of situations other than this MCS (supercells, clear-air echoes, and hurricanes). For the hydrometeor environment, the dominant factors influencing TREC wind retrieval accuracy include the magnitude of vertical wind shear, microphysical factors influencing reflectivity factor changes, and hydrometeor fall speeds. In vigorous convection associated with high-shear situations such as the supercell storm, TREC does very poorly and scatterplots of the TREC radial component versus the measured Doppler velocities typically show low correlation. In situations of low shear in the cloud layer, including the 13 July MCS and hurricanes, TREC appears to provide a good representation of mesoscale winds.

Two methods were used to assess accuracy of the TREC mesoscale flow field estimates. The best comparison of course is a multiple-Doppler radar analysis (Shapiro et al. 1996), which is only possible in part of

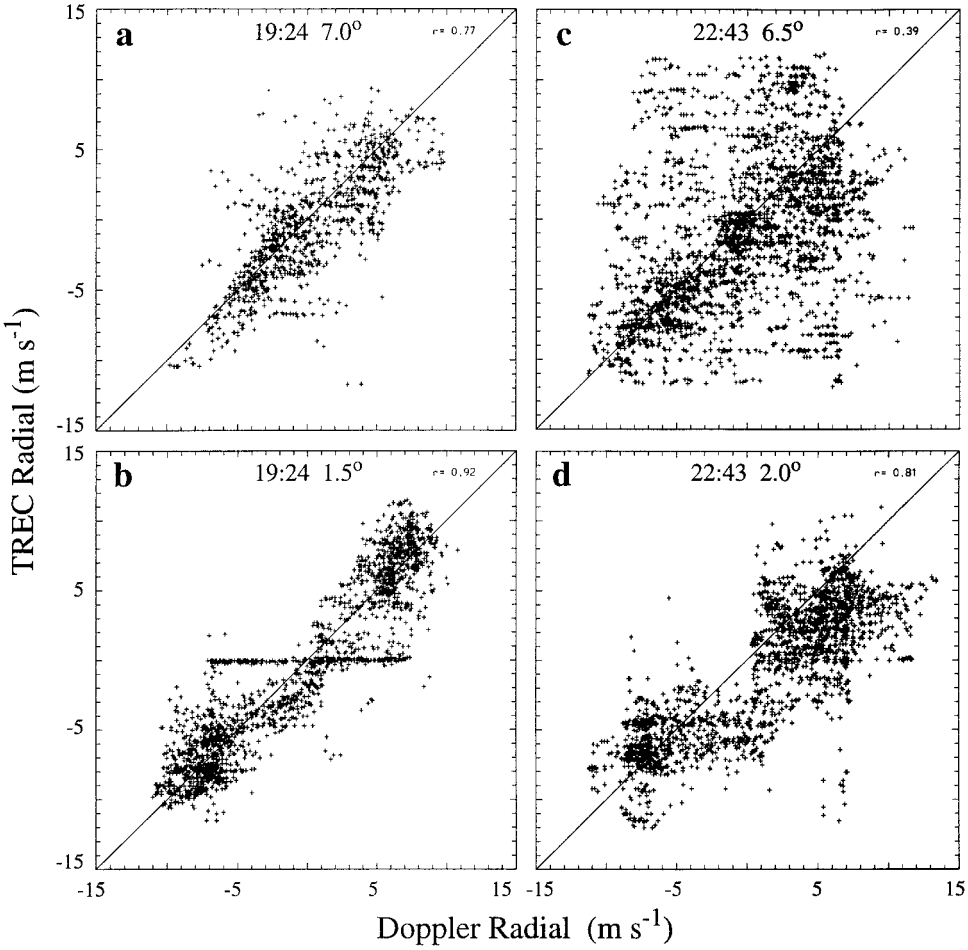

FIG. B1. Scatterplots of Doppler radial velocity against the radial component of the TREC-derived horizontal wind, for CP-4 data in the original polar coordinate system. The diagonal line represents a perfect match, and the correlation coefficient r is given in the upper-right corner. (a) 1924 UTC, for the 360° sweep at an elevation angle of 7°; (b) 1924 UTC, at 1.5°; (c) 2243 UTC, at 6.5°; and (d) 2243 UTC, at 2.0°. The time given marks the beginning of the first of two volumes of radar data.

the domain. We computed the TREC-derived mean wind profile in an area of 200 km × 175 km around CP-4 for the two volumes taken between 1956 and 2005 UTC and compared it against the 2004 UTC MSFC sounding (Fig. I.4b). The absolute mean difference in speed from the 1- to 10-km heights was 1.52 m s^{-1}, and the TREC velocities were biased toward westerly at 0.11 m s^{-1} and toward southerly at 0.68 m s^{-1}. This bias toward southerly is consistent with the observation that the storm moved southward relative to the deep-layer mean wind (Fig. I.4b).

We also compared the radial component of the TREC winds to the Doppler velocities directly measured by CP-4 (Fig. B1). TREC results were most accurate during the earlier time periods from about 1930 to 2100 UTC, with correlations generally exceeding 0.9 at low elevation angles. A histogram of the distribution of the TREC radial and Doppler radial differences shows that at 1926 UTC only about 35% and 12% of the TREC vectors differ from the Doppler measurements by more than 2 and 3 m s^{-1}, respectively. Correlations decreased after about 2230 UTC, particularly at upper levels, as the system became more stratiform with fewer trackable echo features. At 2242 UTC the percentages for the 2 and 3 m s^{-1} differences increased to 45% and 30%, respectively. The deterioration is quite evident not only in the scatterplots, but also in the vector field. However, physically consistent velocity fields were still recovered (Fig. 14).

At very low elevation angles (1.5° and below), many TREC velocities are zero, resulting in a horizontal line cluster in the scatterplot, as seen in Fig. B1. The TREC velocities are zero here because the echo tracking technique is very sensitive to stationary ground clutter. At 2243 UTC the Doppler radial velocity is biased toward positive values (Fig. B1d). Since most echoes are to the south of CP-4 at this time (see Fig. 1b), this positive bias implies a southerly bias; in other words the echoes

no longer propagate southward relative to the layer mean wind.

REFERENCES

Biggerstaff, M. I., and R. A. Houze Jr., 1991a: Kinematic and precipitation structure of the 10–11 June 1985 squall line. *Mon. Wea. Rev.*, **119,** 3035–3065.

——, and ——, 1991b: Midlevel vorticity structure of the 10–11 June 1985 squall line. *Mon. Wea. Rev.*, **119,** 3066–3079.

——, and ——, 1993: Kinematics and microphysics of the transition zone of the 10–11 June 1985 squall line. *J. Atmos. Sci.*, **50,** 3091–3110.

Bluestein, H. B., 1993: *Synoptic–Dynamic Meteorology in Midlatitudes. Volume II: Observations and Theory of Weather Systems*, Oxford University Press, 594 pp.

Bosart, L. F., and F. Sanders, 1981: The Johnstown flood of July 1977: A long-lived convective system. *J. Atmos. Sci.*, **38,** 1616–1642.

Brandes, E. A., 1990: Evolution and structure of the 6–7 May 1985 mesoscale convective system and associated vortex. *Mon. Wea. Rev.*, **118,** 109–127.

Braun, S. A., and R. A. Houze Jr., 1995: Diagnosis of hydrometeor profiles from area-mean vertical velocity data. *Quart. J. Roy. Meteor. Soc.*, **121,** 23–53.

Brooks, H. E., and C. A. Doswell III, 1994: On the environments of tornadic and nontornadic mesocyclones. *Wea. Forecasting*, **9,** 606–618.

Browning, K. A., and R. Wexler, 1968: A determination of kinematic properties of a wind field using Doppler radar. *J. Appl. Meteor.*, **7,** 105–113.

Chong, M., P. Amayenc, G. Scialom, and J. Testud, 1987: A tropical squall line observed during the COPT 81 experiment in West Africa. Part I: Kinematic structure inferred from dual-Doppler radar data. *Mon. Wea. Rev.*, **115,** 670–694.

Fovell, R. G., and Y. Ogura, 1988: Numerical simulation of a midlatitude squall line in two dimensions. *J. Atmos. Sci.*, **45,** 3846–3879.

Fritsch, J. M., J. D. Murphy, and J. S. Kain, 1994: Warm core vortex amplification over land. *J. Atmos. Sci.*, **51,** 1780–1807.

Heymsfield, A. J., 1972: Ice crystal terminal velocities. *J. Atmos. Sci.*, **29,** 1348–1357.

——, and L. J. Donner, 1990: A scheme for parameterizing ice–cloud water content in general circulation models. *J. Atmos. Sci.*, **47,** 1865–1877.

Hobbs, P. V., T. J. Matejka, P. H. Herzegh, J. D. Locatelli, and R. A. Houze Jr., 1980: The mesoscale and microscale structure and organization of clouds and precipitation in midlatitude cyclones. Part I: A case study of a cold front. *J. Atmos. Sci.*, **37,** 568–596.

Houze, R. A., Jr., B. F. Smull, and P. Dodge, 1990: Mesoscale organization of springtime rainstorms in Oklahoma. *Mon. Wea. Rev.*, **118,** 613–654.

Klimowski, B. A., 1994: Initiation and development of rear inflow within the 28–29 June 1989 North Dakota mesoconvective system. *Mon. Wea. Rev.*, **122,** 765–779.

Knollenberg, R. G., K. Kelly, and J. C. Wilson, 1993: Measurements of high number densities of ice crystals in the tops of tropical cumulonimbus. *J. Geophys. Res.*, **98,** 8639–8664.

Knupp, K. R., and V. Chandrasekar, 1993: Estimation of C-band attenuation in heavy rain environments. Preprints, *26th Int. Conf. on Radar Meteorology*, Norman, OK, Amer. Meteor. Soc. 543–545.

——, B. Geerts, and S. J. Goodman, 1998: Analysis of a small, vigorous mesoscale convective system. Part I: Formation, radar echo structure, and lightning behavior. *Mon. Wea. Rev.*, **126,** 1812–1836.

Lafore, J.-P., and M. W. Moncrieff, 1989: A numerical investigation of the organization and interaction of the convective and stratiform regions of tropical squall lines. *J. Atmos. Sci.*, **46,** 521–544.

Leise, J. A., 1981: A multi-dimensional scale-telescoped filter and data extension package. NOAA Tech Memo. WPL-82, 20 pp. [Available from NOAA/ERL/ETL, 325 Broadway, Boulder, CO 80303.]

Lu, Y. Y., R. J. Doviak, and C. Crisp, 1996: Estimating large scale vorticity using VAD products and reflectivity. *J. Atmos. Oceanic Technol.*, **13,** 1129–1138.

Raymond, D. J., and H. Jiang, 1990: A theory for long-lived mesoscale convective systems. *J. Atmos. Sci.*, **47,** 3067–3077.

Rinehart, R. E., 1979: Internal storm motions from a single Doppler weather radar. NCAR/TN-146+STR, 262 pp. [Available from UCAR Communications, P. O. Box 3000, Boulder, CO 80307-3000.]

Rotunno, R., J. B. Klemp, and M. L. Weisman, 1988: A theory for strong, long-lived squall lines. *J. Atmos. Sci.*, **45,** 463–485.

Rutledge, S. A., and R. A. Houze Jr., 1987: A diagnostic modeling study of the trailing stratiform region of a midlatitude squall line. *J. Atmos. Sci.*, **44,** 2640–2656.

——, ——, M. I. Biggerstaff, and T. J. Matejka, 1988: The Oklahoma–Kansas mesoscale convective system of 10–11 June 1985: Precipitation structure and single Doppler radar analysis. *Mon. Wea. Rev.*, **116,** 1409–1430.

Sasyo, Y., 1971: Study of the formation of precipitation by the aggregation of snow particles and the accretion of cloud droplets on snow flakes. *Pap. Meteor. Geophys.*, **22,** 69–142.

Shapiro, A., L. Zhao, J. Zhang, J. Tuttle, S. Laroche, I. Zawadski, Q. Xu, and J. Gao, 1996: Single-Doppler velocity retrievals with hailstorm data from the North Dakota Thunderstorm Project. Preprints, *18th Conf. on Severe Local Storms*, San Francisco, CA, Amer. Meteor. Soc., 546–550.

Skamarock, W. C., M. L. Weisman, and J. B. Klemp, 1994: Three-dimensional evolution of simulated long-lived squall lines. *J. Atmos. Sci.*, **51,** 2563–2584.

Smull, B. F., and R. A. Houze Jr., 1987a: Rear inflow in squall lines with trailing stratiform precipitation. *Mon. Wea. Rev.*, **115,** 2869–2889.

——, and ——, 1987b: Dual-Doppler analysis of a midlatitude squall line with a trailing region of stratiform rain. *J. Atmos. Sci.*, **44,** 2128–2148.

Srivastava, R. C., T. J. Matejka, and T. J. Lorello, 1986: Doppler-radar study of the trailing anvil region associated with a squall line. *J. Atmos. Sci.*, **43,** 356–377.

Tuttle, J. D., and G. B. Foote, 1990: Determination of the boundary layer airflow from a single Doppler radar. *J. Atmos. Oceanic Technol.*, **7,** 218–232.

——, and R. Gall, 1995: Radar analysis of Hurricanes Andrew and Hugo. Preprints, *21st Conf. on Hurricanes and Tropical Meteorology*, Miami, FL, Amer. Meteor. Soc., 608–610.

Verlinde, J., and W. R. Cotton, 1990: A mesoscale vortex couplet observed in the trailing anvil of a multicellular convective complex. *Mon. Wea. Rev.*, **118,** 993–1010.

Weisman, M. L., 1992: The role of convectively generated rear-inflow jets in the evolution of long-lived mesoconvective systems. *J. Atmos. Sci.*, **49,** 1826–1847.

Willis, P. T., and A. J. Heymsfield, 1989: Structure of the melting layer in mesoscale convective system stratiform precipitation. *J. Atmos. Sci.*, **46,** 2008–2025.

Yeh, J. D., M. A. Fortune, and W. R. Cotton, 1986: Microphysics of the stratified precipitation region of a mesoscale convective

system. Preprints, *23d Conf. on Radar Meteorology*, Snowmass, CO, Amer. Meteor. Soc., 151–154.

Yuter, S. E., and R. A. Houze Jr., 1995: Three-dimensional kinematic and microphysical evolution of Florida cumulonimbus. Part III: Vertical mass transport, mass divergence, and synthesis. *Mon. Wea. Rev.*, **123,** 1964–1983.

Zhang, D. L., and K. Gao, 1989: Numerical simulation of an intense squall line during 10–11 June 1985 PRE-STORM. Part II: Rear inflow, surface pressure perturbations, and stratiform precipitation. *Mon. Wea. Rev.*, **117,** 2067–2094.

Ziegler, C. L., 1988: Retrieval of thermal and microphysical variables in observed convective storms. Part II: Sensitivity of cloud processes to variation of the microphysical parameterization. *J. Atmos. Sci.*, **45,** 1072–1090.